Title

Local synthesis of Reticulon-1C lessens the outgrowth of injured axons and Spastin activity

Authors

Alejandro Luarte[1,2,3]*, Javiera Gallardo[8], Daniela Corvalán[1,2], Ankush Chakraborty [1,2], Cláudio Gouveia-Roque[5], Francisca Bertin[11], Carlos Contreras[1,2], Juan Pablo Ramírez [1,2], André Weber [20], Waldo Acevedo[8], Werner Zuschratter[19], Rodrigo Herrera-Molina[9,10], Úrsula Wyneken [1,2,3] , Andrea Paula-Lima [16,17], Tatiana Adasme-Rocha[18], Jorge Toledo[21], Rodrigo Vergara[22] , Antonia Figueroa[1,2], Carolina González[15], Christian González-Billault[4, 12, 13, 14], Ulrich Hengst [5,6], and Andrés Couve [4]

Affiliations

1 Faculty of Medicine, Universidad de los Andes, Santiago 7620001, Chile
2 Program in Neuroscience, Center for Biomedical Research, and Innovation (CiiB), Universidad de los Andes, Santiago 7620001, Chile
3 IMPACT, Center of Interventional Medicine for Precision and Advanced Cellular Therapy, Santiago 7620001, Chile
4 Department of Neuroscience, Faculty of Medicine, Universidad de Chile, Santiago, Chile.
5 The Taub Institute for Research on Alzheimer's Disease and the Aging Brain, Columbia University Vagelos College of Physicians and Surgeons, New York, NY 10032, USA
6 Department of Pathology and Cell Biology, Columbia University Vagelos College of Physicians and Surgeons, New York, NY 10032, USA
7 Instituto de Química, Facultad de Ciencias, Pontificia Universidad Católica de Valparaíso, Valparaíso 2373223, Chile
8 Centro de Medicina Regenerativa, Facultad de Medicina, Clínica Alemana-Universidad del Desarrollo, Santiago, Chile
9 Centro Integrativo de Biología y Química Aplicada, Universidad Bernardo O'Higgins, 8307993 Santiago, Chile
10 Department of Pharmacology & Physiology, George Washington University, Ross Hall, Washington, DC, USA
11 Facultad de Medicina Veterinaria y Agronomía, Universidad de Las Américas, sede Providencia, Manuel Montt 948, 7500975, Santiago, Chile
12 Department of Biology, Faculty of Sciences, Universidad de Chile, Santiago, Chile
13 Public Nutrition Unit, Institute for Nutrition and Food Technologies, Universidad de Chile, Santiago, Chile
14 The Buck Institute for Research on Aging, Novato, USA
15 Latin American Brain Health Institute (BrainLat), Universidad Adolfo Ibañez, Santiago, Chile
16 Biomedical Neuroscience Institute and Department of Neurosciences, Faculty of Medicine, Universidad de Chile, Santiago 8380000, Chile
17 Institute for Research in Dental Sciences (ICOD), Faculty of Dentistry, Universidad de Chile, Santiago 8380544, Chile
18 Oficina de apoyo a la investigación clínica, Hospital Clínico Universidad de Chile, Santiago 8380494, Chile
19 Leibniz Institute for Neurobiology, 39118 Magdeburg, Germany
20 Photonscore GmbH, Brenneckestr. 20, 39118 Magdeburg, Germany
21 Health Sciences Department, Universidad de Aysén, Coyhaique, Chile.
22 Departamento de Kinesiología, Facultad de Artes y Educación Física, Universidad Metropolitana de Ciencias de la Educación

*Corresponding author at: Faculty of Medicine, Universidad de los Andes, Santiago 7620001, Chile. aluarte@uandes.cl

Abstract

The regenerative potential of developing cortical axons depends on intrinsic mechanisms, such as axon-autonomous protein synthesis, that are still not fully understood. An emerging factor in this regenerative response is the bi-directional interplay between microtubule dynamics and the axonal endoplasmic reticulum (ER). We hypothesize that locally synthesized ER proteins regulate microtubule dynamics and the regeneration of cortical axons. RNA data-mining identified the ER-shaping protein Reticulon-1 as a relevant candidate across eight axonal transcriptomes. Using microfluidic chambers, we demonstrate that local knockdown of Reticulon-1 synthesis increases the outgrowth of injured cortical axons while reducing their distal tubulin levels. Furthermore, we show by live-cell imaging that axonal Reticulon-1 knockdown restores the microtubule growth rate and track length modified by injury. Interestingly, local inhibition of the microtubule-severing protein Spastin prevents the axonal knockdown-mediated effects over outgrowth and tubulin levels. We demonstrate that the Reticulon-1C isoform is locally synthesized within axons and support its isoform-specific role in attenuating Spastin-mediated microtubule severing. These findings uncover a mechanism by which axonal protein synthesis finely controls microtubule dynamics and outgrowth upon injury.

Introduction

Developing cortical axons can regenerate after injury but lose this capacity at later stages (Cooke et al., 2022). The transition from a regenerative to a non-regenerative state highlights the importance of identifying the factors that may underlie this shift. The regenerative potential of developing axons depends on extrinsic and intrinsic (cell autonomous) factors that regulate their outgrowth (He & Jin, 2016). The structure of the axonal endoplasmic reticulum (ER) is a determinant intrinsic factor for regulating outgrowth during development and after injury (Aridor & Fish, 2009; Deitch & Banker, 1993; Krijnse-Locker et al., 1995; Nozumi et al., 2009; Petrova et al., 2020; Rao et al., 2016). Indeed, ER proteins are locally synthesized in axons and may contribute to regeneration (Pacheco et al., 2020; Willis et al., 2005). However, the role of axonal protein synthesis in shaping ER function after injury remains largely unexplored.

Unlike the ribosome-rich somato-dendritic ER, the structure of the axonal ER predominantly comprises continuous tubules of smooth ER, maintained by specific ER-shaping proteins (Voeltz et al., 2006; Wu et al., 2017). As such, the mostly tubular axonal ER controls calcium handling, lipid provision, and potentially transmembrane protein supply, which contribute to axon elongation (Cornejo et al., 2017; de Juan-Sanz et al., 2017; González et al., 2016; Luarte et al., 2018). More recently, a bi-directional relationship of the axonal ER with microtubule dynamics has emerged as critical for regulating outgrowth. For instance, the physical coupling of the axonal ER to growing microtubules through STIM1 determines its positioning into filopodia in growth cones to control the guidance of developing axons (Pavez et al., 2019). In turn, the axonal ER controls microtubule dynamics, which is required for axonal specification and proper outgrowth in response to injury (Farías et al., 2019; Rao et al., 2016).

Different lines of evidence support that the protein components of the axonal ER may interact with proteins that regulate microtubule dynamics. For instance, the interaction of ER structural proteins with microtubule severing enzymes may contribute to sculpt the axonal cytoskeleton required for outgrowth (Rao et al., 2016; Stone et al., 2012). As such, the microtubule-severing protein Spastin is known to interact with different ER-shaping proteins (Evans et al., 2006; Mannan et al., 2006), but the contribution of axonal protein synthesis to this process has not been addressed. Here, we hypothesized that the local synthesis of ER structural proteins controls microtubule dynamics and the elongation of injured axons. Using a variety of techniques, we report that local synthesis of the ER-shaping protein Reticulon-1 (Rtn-1) controls microtubule dynamics and the outgrowth of injured cortical axons depending on Spastin-mediated microtubule severing.

Results

Rtn-1 mRNA is consistently identified in axonal transcriptomes

We hypothesized that the local synthesis of an ER structural protein controls microtubule dynamics and the elongation of injured axons. As a first approach to test our hypothesis, we looked for mRNAs coding for ER structural proteins in reported axonal transcriptomes from different species, developmental stages, and days *in vitro* (DIV) as indicated in Table I. To enhance the robustness of our analysis, we focused on transcripts that were consistently identified across conditions using Venn analysis. We identified 104 common mRNAs across all studies (Figure 1A) and classified them under the 'Cellular Component' category using Gene Ontology (GO) analysis. We found that *Rtn-1* mRNA was the only transcript coding for an ER structural protein that is shared across all the samples (Figure 1B). Note that several of the identified transcripts in the category 'endoplasmic reticulum' code for cytoplasmic ribosomal components, which indeed can be attached to the axonal ER (Koppers et al., 2024) and be locally synthesized in axons (Shigeoka et al., 2019). On a similar approach, but combining data from dendrites and axons, it was found that *Reticulon-3* mRNA is present in 16 out of 20 studies, further suggesting a wider presence of other mRNAs coding for ER structural proteins in axons (von Kügelgen & Chekulaeva, 2020). Interestingly, one of the studies presented in (Figure 1B) showed that *Rtn-1* mRNA levels in cortical axons are decreased by 5.26 ± 0.06-fold after axotomy (Taylor et al., 2009). Thus, *Rtn-1* mRNA is consistently identified in axons, and it is down-regulated upon injury.

Next, we studied the distribution of Rtn-1 protein in axons from cultured rat cortical neurons at early developmental stages. To this end, we assessed the fluorescence intensity of Rtn-1 along the terminal 50 µm of distal axons at 1, 3, and 7 DIV. Axonal identity was confirmed by β3-tubulin and the absence of the dendritic marker microtubule-associated protein 2 (MAP2). Rtn-1 fluorescence was concentrated in the most distal axonal region corresponding to the growth cone (GC), which is significantly more pronounced at 7 DIV compared to 1 DIV (Supplementary Figure 1A-C). Rtn-1 enrichment within GCs diverged from the staining pattern of KDEL, a luminal ER marker, which did not exhibit such progressive accumulation (Supplementary Figure 1A-C). The distribution of Rtn-1 agreed with prior studies that localized this protein at the base of the GC's hand-like structure, as outlined by the F-actin cytoskeleton stained with phalloidin (Nozumi et al., 2009) (Supplementary Figure 1D). This distribution supports a model where Rtn-1 contributes to the dense network of ER tubules characteristically found in the GCs, an observation well-documented in earlier studies (Deitch & Banker, 1993)

148 **Axonal synthesis of Rtn-1 lessens outgrowth after injury**

149

150 To elucidate the role of Rtn-1 synthesis in the outgrowth of injured axons, we first
151 validated knockdown (KD) of this protein by Western blot (WB) in cultured cortical neurons.
152 Neuronal Rtn-1 isoforms include isoform A (Rtn-1A), comprising 776 amino acids, and isoform
153 C (Rtn-1C) with 208 amino acids. Both isoforms share a highly conserved C-terminal region
154 known as the Reticulon homology domain (RHD), differing only in their 20 N-terminal amino
155 acids (Chiurchiù et al., 2014; Roebroek et al., 1993). Thus, we transfected 7 DIV dissociated
156 cortical neurons with siRNAs designed to target the conserved RHD domain (i.e., siRNAs that
157 target all Rtn-1 isoforms) or a control sequence (scrambled, Scr). Forty-eight hours later, samples
158 were analyzed using a pan-Rtn-1 antibody raised against the conserved RHD region. Two distinct
159 Rtn-1 bands were observed: a higher molecular weight band near 180 kDa, likely representing
160 Rtn-1A (Van De Velde et al., 1994), and a lower band near 24 kDa, corresponding to the apparent
161 molecular weight of Rtn-1C (Roebroek et al., 1993; Van De Velde et al., 1994) (Figure 2A). When
162 quantifying the 24 kDa band, both siRNAs significantly reduced Rtn-1 levels compared to Scr
163 (Figure 2A). We also examined the 180 kDa band and found that siRNA 1 reduced expression to
164 a mean of 0.41 relative to Scr, showing a strong trend that did not reach statistical significance (p
165 $= 0.05$; $N = 3$; Wilcoxon test compared to 1, data not shown). In contrast, siRNA 2 further reduced
166 expression to a mean of 0.29, which was statistically significant ($p = 0.04$; $N = 3$; Wilcoxon test
167 compared to 1, data not shown). Together, these results indicate that, when considering both
168 isoforms, siRNA 2 achieves the stronger KD. Therefore, unless otherwise indicated, for all
169 subsequent experiments siRNA 2 was used to downregulate Rtn-1. Immunofluorescence staining
170 further revealed a marked decrease in Rtn-1 intensity in the cell body and distal axons of neurons
171 co-transfected with an RFP-expressing plasmid and siRNA 2 under the same recently described
172 conditions (Figure 2B).

173

174 Once we validated the siRNA 2, we aimed at performing KD of Rtn-1 expression
175 selectively within the axonal compartment (axonal Rtn-1 KD) in 7 DIV microfluidic chamber
176 cultures. This compartmentalized approach has been validated in multiple studies to locally
177 control neuronal protein synthesis (Baleriola et al., 2014; Batista et al., 2017; Zhang et al.,
178 2013).Twenty-four hours later, we found that axonal Rtn-1 KD did not alter somatic Rtn-1 levels
179 yet elicited a significant ~ 25% decrease in somatic β3-tubulin, which were quantified as the
180 intensity fold change for both proteins compared to Scr (Figure 2C). Compatible with Rtn-1 local
181 synthesis, axonal Rtn-1 KD led to a significant ~ 46% decrease in its fluorescence intensity within
182 the distal 50 µm of axons, which was depicted by the corrected fluorescence intensity profile and
183 quantified as the intensity fold change compared to Scr (Figure 2D and E). A slight but significant
184 ~ 16% decrease in β3-tubulin fluorescence intensity fold change was also observed after axonal

185 Rtn-1 KD compared to Scr (Figure 2D and E). These results support that local synthesis of Rtn-1
186 can be locally downregulated in the axonal compartment and suggest an interplay with the
187 organization of the microtubule cytoskeleton.
188
189 To investigate the role of local Rtn-1 synthesis in axonal outgrowth, we subjected 8 DIV
190 cortical axons to axotomy by vacuum aspiration in microfluidic chambers. To this end, we
191 simultaneously performed Rtn-1 KD in either axonal or somato-dendritic compartments and
192 measured outgrowth twenty-four hours later (Figure 3A). To measure outgrowth, we took
193 advantage of the semi-circle configuration of the NeuroAnatomy FIJI plugin and performed Sholl
194 analysis (McCurdy et al., 2019; Sholl, 1953). We quantified the summation of the intersections
195 of binarized axons with concentric semi-circles of 2 µm increasing radius starting from the
196 microgroove exit and centered at axonal fields of equivalent size (Figure 3B, top). Interestingly,
197 we observed a significant increase in outgrowth (higher number of intersections summation)
198 within the 500-1000 µm and 1000-1500 µm ranges with axonal Rtn-1 KD compared to Scr
199 (Figure 3B, bottom). Furthermore, this response was specific for the axonal compartment, as
200 somatic Rtn-1 KD showed a non-significant effect with a slight opposite trend (Figure 3C).
201
202 To discard off-target effects of siRNA used for axonal Rtn-1 KD, we validated a third
203 and completely different oligonucleotide sequence (siRNA 3) specifically directed against Rtn-1
204 and tested its capacity to reproduce the observed phenotype with local KD in injured axons. We
205 found by WB that this sequence significantly decreased Rtn-1C levels, while Scr and non-
206 transfected neurons did not. Also, no significant changes of β3-tubulin levels were observed
207 (Supplementary Figure 2A-B). To test the ability of siRNA 3 to promote outgrowth, we
208 selectively treated axotomized axons in microfluidic chambers and measured outgrowth twenty-
209 four hours after injury. Axonal KD performed with siRNA 3 resembled the overall outgrowth
210 tendency observed with siRNA 2 (Figures 3A-B). It was observed a significant increase in the
211 summation of axonal intersections within the 0-500 µm and 500-1000 µm ranges after axonal
212 Rtn-1 KD compared to Scr (Supplementary Figure 2C-D). Together, these results suggest that the
213 increased outgrowth of injured axons observed with axonal Rtn-1 KD is not likely due to siRNA
214 off-target effects.
215
216 To further characterize the role of axonally synthesized Rtn-1 in injured axons, we
217 assessed the morphology of GCs in the same experimental setting described above. To this end,
218 we used β3-tubulin immune staining and phalloidin incubation to reveal the actin cytoskeleton.
219 Axonal Rtn-1 KD did not modify the outline (perimeter) and the area of GCs. However, axonal
220 Rtn-1 KD produced GCs characterized by a more elongated and compact actin cytoskeleton,
221 reflected on a significant increase in the elongation ratio (calculated as the length of the major

222 axis divided by the length of the minor axis of the best-fitting ellipse to the actin boundary) and
223 longest shortest path (LSP, which reflects the maximum length of the skeletonized actin outline),
224 alongside a reduced number of filopodia (Figure 3D). Collectively, these morphometric
225 parameters revealed that axonal Rtn-1 KD yielded GCs resembling a spade-like morphology that
226 has been previously related to increased outgrowth (Kaethner & Stuermer, 1992). Compatible
227 with this idea, somatic Rtn-1 KD did not promote outgrowth nor modified any of these
228 morphological parameters, except for an increase in the GC LSP (Figure 3D). Together, these
229 results suggest that axonal synthesis of Rtn-1 is normally acting to repress the outgrowth of
230 injured axons.
231
232 **Axonal Rtn-1 KD decreases β3-tubulin levels in injured axons**
233
234 The previously described changes in β3-tubulin elicited by axonal Rtn-1 KD before injury
235 (Figure 2D), lead us to examine β3-tubulin and Rtn-1 fluorescence intensity under this condition
236 in axotomized axons. Different from what we observed in intact axons (Figure 2D and E), twenty-
237 four hours of axonal Rtn-1 KD did not alter Rtn-1 fluorescence significantly, but it induced a ~
238 20 % reduction in β3-tubulin intensity compared to Scr (Figure 4A). In contrast, somatic Rtn-1
239 KD did decrease Rtn-1 fluorescence in axons by ~ 33% (Figure 4B), supporting the notion that
240 most of axonal Rtn-1 protein originates in the soma. Of note, somatic Rtn-1 KD also decreased
241 β3-tubulin intensity by ~ 19% in axons (Figure 4B).
242
243 Consistent with a potential compensatory response of the cell body upon injury, axonal
244 Rtn-1 KD leads to increased somatic Rtn-1 fluorescence compared to Scr (Figure 4C).
245 Interestingly, an isoform-specific increase in Rtn-1C levels has been previously described upon
246 the injury of cortical neurons (Fan et al., 2018). Despite we still do not know the mechanism, the
247 somatic increase that we observe may partially explain the lack of changes in axon Rtn-1 levels
248 after twenty-four hours of axonal KD (Figure 4A), which is potentially countered by somatic Rtn-
249 1 synthesis. Intriguingly, resembling the somatic increase of Rtn-1, β3-tubulin levels were also
250 elevated in the cell bodies following axonal Rtn-1 KD compared to Scr (Figure 4C). In contrast,
251 somatic Rtn-1 KD resulted in a significant reduction in the somatic fluorescence intensity for both
252 proteins compared to Scr (Figure 4D). Together, these results indicate that after axonal injury, the
253 levels of Rtn-1 in the somatic and axonal compartments tend to change in a manner that parallels
254 β3-tubulin, which suggests a mechanistic relationship between these two proteins.
255
256
257
258

Spastin activity regulates β3-tubulin and axon re-growth under local Rtn-1 KD

The significant alterations in β3-tubulin levels after Rtn-1 KD in the context of injury, led us to explore the role of Rtn-1 interactors that can modify the microtubule cytoskeleton. Notably, a previous study had shown by yeast two hybrid assay that a protein sequence from Rtn-1C directly interacts with the microtubule-severing protein Spastin (Mannan et al., 2006). Therefore, we explored the localization of Spastin and Rtn-1C in distal axons before and after injury.

To this end, we stained 9 DIV non-injured and injured axons (submitted to axotomy at 8 DIV) against Spastin (all isoforms) and Rtn-1C to perform Stimulated Emission Depletion (STED) super-resolution microscopy. In both conditions, Rtn-1C and Spastin showed enrichment of the staining in the GC (Figure 5A, left panel). The distribution of Rtn-1C along the axonal shaft is fine and continuous, consistent with its localization in ER tubules, which appear decorated with clusters of Spastin. In contrast to the more central positioning of Rtn-1C in the axonal shaft, Spastin displays a broader distribution in both conditions (Figure 5A, left panel). This difference is also seen in the GCs, where Rtn-1C is more concentrated at the center of these domains (Figure 5A, left panel). In injured axons, distal Rtn-1C staining appears less compact, adopting a more tubulated pattern (Figure 5A, left panel). Moreover, following injury, Rtn-1C staining seems slightly retracted from the GC compared to the non-injured condition, as also suggested by its relative intensity profile (Figure 5A, right panel). Spastin distribution along the distal axon remains similar between conditions (Figure 5A, right panel). However, in injured axons, Spastin appears less diffuse and more concentrated in clusters than in non-injured axons (Figure 5A left and right panel). No significant changes were observed when analyzing the total fluorescence intensity of both proteins (Supplementary Figure 4). These findings suggest that both proteins are closely apposed in the GC and along the axonal shaft. Although we did not directly test their direct molecular association, these results are consistent with Rtn-1C and Spastin sharing a similar subcellular localization, potentially enabling their functional interaction in distal axons.

To further investigate the role of these proteins, we subjected 8 DIV cortical axons to axotomy by vacuum aspiration in microfluidic chambers. Under these conditions, we aimed at elucidating the potential connection of Rtn-1 axonal synthesis KD with Spastin's microtubule-severing activity. To this end, we took advantage of a Spastazoline (SPTZ), a well-characterized and specific inhibitor of the ATPase activity of Spastin (i.e., microtubule severing)(Cupido et al., 2019). Under these conditions, we monitored the changes in the fluorescence intensity of β3-tubulin, Rtn-1C, and Spastin in distal axons forty-eight hours after injury. Note that these experiments were performed in a two-fold longer period compared to those shown in Figure 4. This extended time was taken to i) reveal more clearly the changes in β3-tubulin content and ii)

296 allow the proper expression of the EB3-GFP plasmid which is used for the live-cell imaging
297 described later in Figure 5. We found that axonal Rtn-1 KD resulted in a ~ 60% reduction in β3-
298 tubulin levels within the distal 50μm of axons, compared to controls (Scr + DMSO) (Figure 5B).
299 However, co-incubation with 50 nM SPTZ (applied four hours after axotomy) completely
300 abolished the β3-tubulin reduction elicited by axonal Rtn-1 KD, while it did not alter Rtn-1C and
301 Spastin levels (Figure 5B). This rescue of β3-tubulin levels during axonal Rtn-1 KD by a specific
302 drug (SPTZ), makes it unlikely an off-target effect of the siRNA over *β3-tubulin* mRNA. If this
303 was the case, this potential off-target effect should be still operating in the presence of SPTZ.
304 Also discarding unspecific effects over other proteins, SPTZ administration alone did not
305 significantly modify β3-tubulin levels, nor those of Rtn-1C and Spastin (Figure 5B). Together,
306 these observations suggest that axonal Rtn-1 KD correlates with higher Spastin microtubule
307 severing.
308
309 Next, we aimed at exploring whether the increased outgrowth elicited by axonal Rtn-1
310 KD after injury depended on Spastin's microtubule severing. To this end, we studied the effects
311 of axonal Rtn-1 KD on outgrowth forty-eight hours after axotomy by Sholl analysis. In contrast
312 with the effects observed after twenty-four hours of axotomy (Figure 3A), after forty-eight hours
313 of axonal Rtn-1 KD there was only a trend (non-statistically significant) to increase outgrowth in
314 the 1000-1500 μm range compared to controls (Figure 5C and D). However, local co-incubation
315 of 50 nM SPTZ with axonal Rtn-1 KD abolished this trend, producing a statistically significant
316 outgrowth decrease compared to the axonal Rtn-1 KD + DMSO condition (Figure 5 C and D).
317 Local SPTZ application in axons treated with a Scr sequence displayed a trend to increase
318 outgrowth compared to all the conditions, particularly in the 1000-1500 μm segment, but any of
319 these comparisons reached statistical significance (Figure 5C and D). Together, these results
320 suggest that locally synthesized Rtn-1 normally acts to suppress the outgrowth of injured axons,
321 a process that could involve the microtubule-severing activity of Spastin.
322
323 Considering the observed shifts in microtubule content and the previously reported role
324 of Spastin in controlling microtubule stability (Aiken & Holzbaur, 2024; Kuo et al., 2019; Teixeira
325 Lopes, 2018), we aimed at quantifying microtubule dynamics by live-cell imaging before and
326 after injury. To this end, cortical neurons cultured in microfluidic chambers were transfected at 7
327 DIV with a plasmid coding for the microtubule tip-binding protein EB3 fused to the fluorescent
328 construct Emerald GFP (EB3-GFP), which labels the growing plus-ends of polymerizing
329 microtubules (Stepanova et al., 2003). Next, axotomy was performed at 8 DIV microfluidic
330 chambers, and immediately, axons were locally transfected with a Rtn-1 siRNA or Scr sequence.
331 Non-injured 8 DIV axons were transfected in parallel. Four hours after transfection, non-injured
332 and injured axons were either treated with DMSO (vehicle) or 50 nM SPTZ. Then forty-eight

333 hours since injury (at 10 DIV), axons were directly imaged in microfluidic chambers to examine
334 the dynamic behavior of EB3-GFP puncta (comets).
335
336 We first analyzed the effect of axonal Rtn-1 KD on non-injured axons. Interestingly, we
337 found that axonal Rtn-1 KD elicited a statistically significant increase in microtubule growth rate,
338 while it did not significantly modify microtubule track length and lifetime compared to controls
339 (Scr + DMSO) (Figure 5E). To reveal the role of Spastin's microtubule severing in modifying
340 these parameters, we co-incubated axons with 50 nM SPTZ. As such, SPTZ treatment did not
341 prevent the increase in microtubule growth rate elicited by axonal Rtn-1 KD nor modified comet's
342 lifetime but induced a significant increase in track length when compared to controls (Figure 5E).
343
344 Next, we analyzed the effect of axonal Rtn-1 KD on comet parameters after injury. In
345 contrast with the milder increase observed in non-injured axons, axonal Rtn-1 KD augmented by
346 nearly two-fold the growth rate and track length of microtubules, while it did not modify comet
347 lifetime compared controls (Figure 5E, left and right panels). Of note, compared to non-injured
348 axons, growth rate and track length are significantly decreased on axotomized axons (from 0.09
349 to 0.06 µm/s, and from 4.6 µm to 2.6 µm; $p<0.0001$, Mann Whitney test). These results are
350 compatible with axonal damage promoting a more unorganized or less processivity of
351 microtubule growth (Rolls et al., 2020; Yap et al., 2017). SPTZ co-treatment did not prevent the
352 increase in microtubule growth rate and track length elicited by axonal Rtn-1 KD after injury
353 compared to controls, nor modified comet's lifetime (Figure 5E, right panels). However, SPTZ
354 treatment along with axonal Rtn-1 KD did induce a significant increase in comet lifetime when
355 compared to axonal Rtn-1 KD + DMSO as shown in right panels of Figure 5E. Together, these
356 results suggest that axonal Rtn-1 synthesis controls microtubule dynamics in both non-injured
357 and injured axons, for the most part independently of Spastin-mediated microtubule severing.
358
359 Collectively, these results suggest that Rtn-1 would counteract Spastin function locally
360 in axons, impacting on outgrowth. Previous evidence points to a specific role for the Rtn-1C
361 isoform in this potential interplay (Mannan et al., 2006). However, it is still unclear which Rtn-1
362 isoform is locally produced in axons.
363
364
365
366
367
368
369

370 **The Reticulon-1 isoform C (Rtn-1C) is locally synthesized in cortical axons**
371
372 We sought to characterize the isoform expression of *Rtn-1* mRNA and protein in both
373 axons and cell bodies. Because microfluidic chambers yield only limited cellular material, we
374 adopted an alternative culture approach using "neuronballs." This method enables the segregation
375 of an axon-enriched fraction by mechanically separating axons from somato-dendritic structures.
376 The axonal compartment of desomatized neuronballs was identified by IF against medium chain
377 neurofilament (NF-M), while the somato-dendritic compartment was stained with microtubule-
378 associated protein 2 (MAP2) (Figure 6A). RNA was then extracted from both the axonal and
379 somato-dendritic fractions and submitted to reverse transcription PCR (RT-PCR). The purity of
380 the axonal fraction was evidenced by the absence of amplification for *Map2*, *Histone h1(*general
381 nuclei marker), and the astrocyte-specific glial fibrillary acidic protein (*Gfap*) mRNAs. In
382 contrast, we found positive amplification for *β-actin* transcript, which is known to be present in
383 axonal compartment (Figure 6A). These fractions were further analyzed with *Rtn-1* specific
384 primers targeted against C-terminal domain or the N-terminal domain (to reveal *Rtn-1A*). In
385 contrast to the somato-dendritic fraction, axons did not amplify for *Rtn-1A* mRNA, suggesting
386 that *Rtn-1C* transcript is the predominant isoform in this compartment (Figure 6A).
387
388 Next, we investigated the protein composition of the axonal and somato-dendritic
389 fractions of neuronballs by WB. Consistent with the sample purity observed for mRNAs, the
390 axonal fraction was positive for Tau and β3-tubulin, with no detection of the dendritic marker
391 MAP 2 (Figure 6A). For Rtn-1 identification, we employed a pan-Reticulon-1 antibody targeting
392 the conserved C-terminal Reticulon homology domain (RHD). Importantly, the axonal fraction
393 showed exclusivity for the lower molecular weight band, indicative of Rtn-1C presence, mirroring
394 RT-PCR results (Figure 6A). Immunofluorescence analysis of Rtn-1C in axons from 8 DIV
395 microfluidic chambers, displayed a distribution pattern consistent with that of the pan-Reticulon-
396 1 (Rtn-1 antibody), as illustrated in Figure 2 (Figure 6B). In contrast, Rtn-1A presence was limited
397 to a small subset of axons, exhibiting a peak of localization near the growth cone base (Figure
398 6B). Thus, resembling the distribution of transcripts, Rtn-1C protein appears as the predominant
399 isoform in the axonal compartment.
400
401 In Figure 2 we provided evidence compatible with the axonal synthesis of Rtn-1 in
402 cortical axons. In addition, we showed that the predominant mRNA and protein in cortical axons
403 correspond to the Rtn-1C isoform (Figure 6A and B). However, whether Rtn-1C is indeed locally
404 synthesized in cortical axons has not been proved.
405

406 To demonstrate the local production of Rtn-1C in axons, we employed a proximity
407 ligation assay integrated with puromycylation (puro-PLA) (Dieck et al., 2015). During this assay,
408 we selectively administered a puromycin pulse (15 minutes) to the axonal or somato-dendritic
409 compartment of microfluidic chambers, allowing its covalent incorporation into nascent
410 polypeptides. This enabled the detection of newly synthesized Rtn-1C peptides through
411 fluorescent signals produced by the nanometric proximity (<40 nm distance) of puromycin and
412 Rtn-1C antibodies (Figure 6C). Positive amplification was observed in the somato-dendritic
413 compartment of microfluidic chambers with local puromycin treatment as dots or puncta (Figure
414 6D, left panel). However, virtually no signal was detected in the cell bodies when puromycin was
415 added to the axonal compartment, showing the effective compartmentalization of this approach
416 (Figure 6D, left panel). Positive signal in the cell bodies was abrogated when the protein synthesis
417 inhibitor emetine was previously added, further supporting that these signals reflect protein
418 synthesis (Figure 6D, left panel). Supporting its axonal synthesis, fluorescent puncta were
419 observed in axons, which was significantly reduced by previous emetine treatment (Figure 6D,
420 right panel). Interestingly, when the puromycin pulse was applied exclusively to the somatic
421 compartment, positive signal was still detected in axons in a significantly lower amount compared
422 to direct and puromycin treatment, but higher than the emetine/puromycin condition (Figure 6D,
423 right panel). This suggests that at least a fraction of puromycylated peptides synthesized in the
424 cell bodies may rapidly (within 15 minutes) reach the axons through as-yet uncharacterized
425 mechanisms. Nevertheless, the significantly stronger signal detected in the axonal compartment
426 with direct puromycin treatment is fully consistent with local Rtn-1C synthesis in axons.
427
428 To further validate puro-PLA detection, we tested the Rtn-1C antibody specificity by WB
429 and IF, and whether puro-PLA signals depended on local depletion of *Rtn-1* mRNA (axonal Rtn-
430 1 KD). Due to their low background for neuronal components, we used COS-7 cells expressing
431 the rat Rtn-1C protein fused to GFP (Rtn-1C-GFP) and analyzed them by WB, using the same
432 Rtn-1C antibody of the puro-PLA experiment. As expected, a single band of the predicted
433 molecular weight for the recombinant protein was observed in the lane of transfected cells, while
434 no band was apparent in non-transfected cells (Supplementary Figure 3A). Also, revealing an
435 isoform-specific immunodetection, the ER pattern depicted by Rtn-1C-GFP fully overlapped with
436 the IF using the Rtn-1C antibody (Supplementary Figure 3B). Similar results were observed for
437 Rtn-1A-GFP expressing COS-7 cells stained against Rtn-1A antibody (Supplementary Figure
438 3B). Of note, when we performed crossed antibody staining of Rtn-1 isoforms on transfected
439 cells, no positive staining was found (Data not shown). We also tested the specificity of this
440 antibody by transfecting cells with siRNA 2 sequence. As expected, siRNA 2 induced a
441 significant decrease of Rtn-1C band compared to Scr (Supplementary Figure 3C). We also
442 validated the presence of *Rtn-1* mRNA in axons of similar conditions (9 DIV microfluidic

443 chamber) as shown by supplementary Figure 3D. Finally, 9 DIV axons were locally treated in
444 microfluidic chambers with siRNA 2 for twenty-four hours, which produced a significant
445 decrease of positive puro-PLA signal compared to Scr (Supplementary Figure 3D, right).
446 Together, these results confirm that the quantified puro-PLA signal is reflecting the local
447 translation of *Rtn-1C* mRNA in axons.
448
449 **Rtn-1C but not Rtn-1A reduces the microtubule severing activity of Spastin**
450
451 We established that Rtn-1C is locally synthesized in cortical axons, while Rtn-1A
452 synthesis should predominantly occur in the cell body. Therefore, we sought to understand the
453 functional implications of such compartmentalization. We chose COS-7 cells as a heterologous
454 system because of their increased co-transfection efficiency, flat and extended morphology, and
455 low background of neuronal proteins. These features provided an advantageous context to
456 visualize ER protein distribution and functional relationships.
457
458 Thus, we first over-expressed in COS-7 cells an RFP-tagged version of the most abundant
459 Spastin isoform during neuronal development, which corresponds to M87 isoform. Of note, in
460 contrast to M1 isoform, M87 isoform is expected to be soluble and devoid of the ER-shaping
461 membrane domain (Solowska et al., 2017). Next, the plasmid coding for isoform M87 was co-
462 transfected with Rtn-1C-GFP, Rtn-1A-GFP or GFP alone. Spastin-RFP displayed a punctate
463 distribution when co-expressed with GFP, indicative of its potential interaction with endosomal
464 components, as reported elsewhere (Allison et al., 2013) (Figure 7A, upper panels). Under this
465 condition, Spastin puncta strongly co-distributed with some clusters of soluble GFP. It has been
466 described that under certain circumstances soluble proteins such as GFP might be bulk up taken
467 by late endosomal structures (Sahu et al., 2011), which are also known to be positive for M87
468 Spastin (Allison et al., 2019). To rule out that, in our case, this co-distribution is due to
469 fluorescence crosstalk, we independently acquired images for each fluorophore in co-transfected
470 cells. We observed that COS-7 cells co-transfected with Spastin-RFP and GFP displayed the same
471 previously described puncta for both channels, discarding crosstalk (Supplementary Figure 5).
472 Further discarding unspecific channel bleeding, some cells that exclusively express Spastin-RFP,
473 harbor puncta that are exclusively seen in one channel, as indicated in supplementary Figure 5.
474 Similarly, some strong GFP puncta (indicated in the image) are not detected in the RFP channel
475 (Supplementary Figure 5). Complementary, cells co-transfected with Rtn-1A-RFP and GFP show
476 distinct distribution patterns without overlapping puncta, suggesting that the punctate distribution
477 of GFP is associated exclusively with Spastin co-expression and not explained by unspecific
478 bleeding (Supplementary Figure 5).
479

480 Of note, Spastin-RFP pattern was drastically altered when co-expressed with Rtn-1C-
481 GFP (Figure 7B, middle panels). As such, and potentially compatible with their previously
482 reported direct interaction, Spastin closely followed the Rtn-1C pattern distribution (Figure 7B,
483 middle panels). Conversely, Rtn-1A-GFP showed minimal overlap with Spastin-RFP (Figure 7B,
484 lower panels). Quantification of protein colocalization by Mander's coefficients substantiated
485 these observations (Figure 7C).
486
487 Notably, the co-expression of Spastin-RFP with Rtn-1C-GFP maintained tubulin levels
488 unaltered when compared to non-transfected cells from each experimental condition, in marked
489 contrast with their GFP and Rtn-1A-GFP counterpart (Figure 7B and C). Furthermore, the
490 filamentous distribution of tubulin was clearly preserved with Spastin-RFP/ Rtn-1C-GFP co-
491 expression, which is a strong indicative of limited severing of microtubule filaments (Figure 7B,
492 middle panels). These effects cannot be attributed to differences in transfection efficiency, as
493 fluorescence intensity of Spastin-RFP and GFP constructs did not significantly differ across
494 conditions (Supplementary Figure 5). Therefore, these results suggest that the tight co-distribution
495 of Rtn-1C with Spastin is associated with reduced microtubule severing activity, which is not
496 observed for the Rtn-1A isoform.
497
498 The examination of the sequences of Rtn-1C and 1A reveals a unique N-terminal variance
499 as the point of differentiation between both isoforms, as they share their RHD region (Figure 7D).
500 Considering the limited colocalization of Rtn-1A with Spastin (Figure 7B, lower panels), RHD
501 appears not to be sufficient for their interaction. This observation hints at the exclusive 20 N-
502 terminal amino acids of Rtn-1C as being critical for Spastin binding. Therefore, we performed *in*
503 *silico* modeling of the Rtn-1C N-terminal and anticipated its affinity with the microtubule-binding
504 domain (MTBD) of Spastin. This domain showed larger interaction energies compared to the
505 endosome (Microtubule Interacting and Trafficking domain, MIT) and microtubule severing
506 domain (ATPases Associated with diverse cellular Activities, AAA) (Figure 7E). Furthermore,
507 the affinity of a Rtn-1A equivalent region for these domains was also less thermodynamically
508 favored compared to Rtn-1C (Figure 7E). These results are compatible with previous evidence
509 showing that deletion of Spastin's MIT domain, and most of the MTBD region, abrogates Spastin-
510 Rtn-1C co-precipitation(Mannan et al., 2006). This suggests that Rtn-1C binding to Spastin
511 MTBD is competing with the binding of this domain to microtubules. Mechanistically, this would
512 prevent the ring conformation around microtubule filaments required for the severing activity of
513 Spastin(Roll-Mecak & Vale, 2008). Overall, these findings reveal that Rtn-1C, but not Rtn-1A,
514 closely associates with Spastin, leading to a reduction in its microtubule severing activity.
515

516 **Discussion**

517

518 This study uncovers a mechanism whereby downregulation of the local synthesis of the
519 ER protein Rtn-1 promotes the outgrowth of injured cortical axons and microtubule dynamics.
520 Collectively, our results suggest that this enhancement depends on the shielding effect that
521 axonally synthesized Rtn-1C exerts over Spastin microtubule severing. Using this mechanism,
522 cortical neurons may precisely and locally control outgrowth after injury. This finely tuned
523 response after damage is intriguing given that its halting effect on outgrowth may seem, at first
524 sight, detrimental for proper regeneration. However, we may speculate that limiting microtubule
525 turnover at injury site helps axons to accumulate molecular components required for a successful
526 injury repair. In any case, it would be interesting to explore whether local synthesis of Rtn-1 offers
527 a potential therapeutic pathway to enhance regeneration by unleashing its shielding effect over
528 Spastin locally in axons.

529

530 **Control of Rtn-1 synthesis as an adaptive mechanism for axonal injury.**

531 It would also be interesting to further explore whether developing neurons decrease
532 axonal *Rtn-1* mRNA translation as a mechanism to promote outgrowth during development and
533 after damage. For instance, a previous study using axotomized 10 DIV rat cortical neurons in
534 microfluidic chambers found a decrease on *Rtn-1* mRNA levels compared to non-injured axons
535 (Taylor et al., 2009). This reported reduction may also imply that injured axons do not harbor
536 enough *Rtn-1* mRNA to support local synthesis, which would modify the interpretation of our
537 post-injury results. Still, the observed similarity between specific phenotypes before and after
538 injury, including decrease in distal β3-tubulin levels and increased microtubule growth rate are
539 compatible with Rtn-1C synthesis occurring before and after injury. A more definite answer might
540 be provided by performing puro-PLA measurements of Rtn-1C synthesis before and after injury,
541 which is an ongoing work.

542 Currently, it is unknown to what extent a similar mechanism is retained in adult cortical
543 neurons. Likewise, we do not know whether this phenomenon is fully operative *in vivo,* even
544 though *Rtn-1* mRNA is consistently found *in vitro* and *ex vivo*. Of note, *Rtn-1* mRNA is
545 dynamically regulated in the axonal translatome of retinal ganglion cells *in vivo* (Shigeoka et al.,
546 2016), but the functional implications of axonal Rtn-1 synthesis in a more physiological context
547 are yet to be elucidated. Interestingly, growing axonal tips from injured nerves in Lamprey are
548 nearly 13-fold enriched in *Spastin* mRNA, suggesting that other constituent of our described
549 mechanism may be locally synthesized after injury (Jin et al., 2022).

550

551 The presence of the axonal ER (particularly the smooth ER) is thought to be critical for
552 promoting the regeneration of injured neurites by providing membranes and controlling calcium
553 and microtubule dynamics required for outgrowth (Luarte et al., 2018). This has been supported
554 by evidence showing the distribution of smooth ER markers, including ER-shaping proteins such
555 as Reticulons, REEPs, Atlastin, and Spastin isoforms, preferentially at the distal tip of
556 regenerating neurites (Rao et al., 2016; Stone et al., 2012). Indeed, Reticulons share RHD with
557 REEPs, some Spastin isoforms, and Atlastins, which makes them suitable to shape the mostly
558 tubular smooth ER (Chiurchiù et al., 2014; Iwahashi et al., 2007). Highlighting their functional
559 relevance, forcing the localization of smooth ER into axonal tips by the over-expression of the
560 ER membrane protein Protrudin enhances outgrowth of CNS axons (Petrova et al., 2020).
561
562 Different studies have shown that the presence of the axonal ER is associated with the
563 fine-tuning of microtubules stability to sustain axonal extension (Farías et al., 2019; Lee et al.,
564 2009). Our results support a model where axonal outgrowth after injury is restricted by reducing
565 the microtubule growth processivity (reflected by track length), which might be controlled by
566 locally synthesized Rtn-1C. As such, axonal KD of *Rtn-1C* mRNA may set an optimal range of
567 microtubule growth, resembling the beneficial role observed with the treatment of low-dose
568 microtubule stabilizers in axonal regeneration (Brizuela et al., 2015; B. Liu et al., 2023). These
569 results would explain why we observed a trend (yet non-significant) of SPTZ to increase
570 regeneration when applied alone locally in axons (Figure 5C-D). The opposite trend observed
571 with the SPTZ+ Rtn-1 siRNA condition highlights the specificity of this response, pointing that
572 microtubule stability has a relatively narrow optimal range to promote outgrowth (Sengottuvel et
573 al., 2011).

574 Some studies have pointed to a non-canonical role for Rtn-1C synthesis by signaling in
575 the nucleus, potentially through DNA binding and histone deacetylase inhibition (Nepravishta et
576 al., 2010, 2012). It is tempting to speculate that these still emerging roles may also contribute to
577 the observed phenotypes. Of note, different axonally synthesized proteins exert transcriptional
578 control after in response to injury or local cues (Twiss et al., 2016).

579 The differential injury response in axonal outgrowth observed after somatic or axonal
580 Rtn-1 KD, emphasizes the unique molecular and structural environments of axons versus cell
581 bodies. This difference might be explained by at least two scenarios. First, we used a Rtn-1 siRNA
582 that is directed against the conserved RHD sequence; thus, it also targets the Rtn-1A isoform. For
583 instance, we observed limited co-distribution of Rtn-1A with Spastin compared to Rtn-1C, and
584 its N- terminal recruits other signaling pathways (Kaya et al., 2013). Therefore, the observed
585 differential response might be due to the predominant presence of Rtn-1C in axons, while both
586 isoforms are present in the cell bodies. Secondly, increased microtubule severing after axonal

587 Rtn-1 KD might promote outgrowth when coupled to predominantly outward-directed growing
588 filaments that characterize axons, but not with the radial or mixed orientation of microtubules in
589 the cell bodies and dendrites(Baas et al., 2016). Interestingly, global KD of Rtn-1 in developing
590 cortical neurons decreases axonal outgrowth (Nozumi et al., 2009), further supporting the
591 relevance understanding this compartmentalized response.

592 **The role of Spastin's microtubule severing on outgrowth after injury**

593 The positive relationship that we observed between increased Spastin-severing activity
594 and the outgrowth of injured axons may seem counter-intuitive. However, microtubule severases,
595 such as Spastin or Katanin, are known to increase the microtubule filament mass and growth
596 under certain conditions. Indeed, under certain conditions Spastin can stabilize newly produced
597 microtubule tips, paradoxically yielding a net increase in microtubule mass (Kuo & Howard,
598 2021). Furthermore, Spastin tends to concentrate at the tip of growing microtubules to behave as
599 a dual enzyme that cleaves but also stabilizes them after cutting (Kuo et al., 2019). This
600 stabilization property may also partially explain why we observed that the axonal inhibition of
601 Spastin by SPTZ alone tends to promote outgrowth after injury (Figure 5C-D).

602 Collectively, our results might be compatible with axonal Rtn-1 KD releasing Spastin
603 molecules to sever more microtubules, and thus, potentially promote a net increase in filament
604 growing ends and mass. In agreement with this speculation, inhibition of axonal tyrosine ligase
605 (which favor dynamic microtubule ends) impedes outgrowth in injured axons from dorsal root
606 ganglion (Song et al., 2015). Analogously, when Fidgetin (a severing enzyme of microtubule
607 labile ends) is depleted in neurons, axonal regeneration is improved (Matamoros et al., 2019).

608 Like other studies, we observed that increased axonal outgrowth correlates with dynamic
609 microtubule parameters such as growth rate (Liz et al., 2014). However, others have shown that
610 the dynamic properties of microtubules, including microtubule growth rate and track length, can
611 adapt to different outgrowth scenarios, with low capacity to predict axonal extension (Kiss et al.,
612 2018). Thus, controlling dynamic parameters of microtubules is not the only factor that
613 determines the outgrowth capacity of injured axons. The exact mechanisms by which locally
614 synthesized Rtn-1C controls dynamic parameters of microtubules remains unsolved as they seem
615 not to rely on Spastin severing activity. Other Spastin-independent interactions of Rtn-1 may
616 depend on its presence on the tubular ER, which includes the control of functional contacts with
617 mitochondria and autophagosomes (D' Eletto et al., 2019; Reali et al., 2015), but their
618 implications for microtubule dynamic parameters and axonal extension also remain to be solved.

619 Decreasing axonal Rtn-1C translation or increasing Spastin microtubule severing locally
620 in axons may constitute an emerging mechanism for promoting injury recovery. For instance,
621 local application of recombinant Spastin together with polyethylene glycol increases recovery

after sciatic nerve injury (Y. F. Lin et al., 2019). Furthermore, local augmentation of axonal Spastin by the pharmacological local regulation of 14-3-3 promotes the recovery of spinal cord injury (Q. Liu et al., 2024) . Indeed, axonal regeneration is particularly sensitive to the absence of Spastin (Stone et al., 2012). Similarly, results in drosophila show that Spastin gene dosage is particularly relevant for the regenerative response of axons (Stone et al., 2012) .

Implications for length-dependent axonopathies and injury response

The failure of ER shaping protein-function potentially participates in the etiology of multiple length-dependent axonopathies such as hereditary spastic paraplegias (HSPs) (Blackstone et al., 2011). Here, we have described an emerging mechanism relating Rtn-1C with the activity of Spastin, which is the most frequently mutated isoform in HSP (Hazan et al., 1999; Mannan et al., 2006). As a second point of analysis, most of the studies performed to understand axonopathies and axonal damage have focused on a "cell-body-centered view" for protein synthesis and ER function. However, increasing evidence supports the relevance of axonal autonomous response to injury or cues from the local brain microenvironment (Jung et al., 2014; Lopez-Verrilli et al., 2013; Zhang et al., 2013, 2015). Similarly, our work underscores a highly local injury adaptation, which is in harmony with the astonishing extension of central nervous system's axons (H.-M. Lin et al., 2018). These results may provide understanding of axonal pathologies and injury response with a special focus on the autonomous response of cortical axons.

Materials and Methods

Animals and surgical procedures. Pregnant Sprague–Dawley rats at embryonic day 18 were obtained from the Central Animal Facility of Universidad Católica de Chile and euthanized in accordance with the guidelines of the Agencia Nacional de Investigación y Desarrollo de Chile (ANID). All the experimental the procedures were approved by the Institutional Bioethics Committee of Universidad de los Andes (CEC2022106).

Neuron cell cultures. Cortical neurons were cultured from 18-day embryos like previously reported (Deitch & Banker, 1993). Dissociated primary cortical neurons (20,000-30,000 cells) were seeded on glass coverslips coated with 0.1 mg/mL poly-L-lysine (Sigma-Aldrich, P4707). Microfluidic chambers were prepared as previously reported (Taylor et al., 2005). Chambers harboring axonal and somatic compartment connected with 750 μm long microgrooves were mounted over a squared 25 mm glass coverslip previously coated with 0.1 mg/mL poly-D-lysine (Corning, 354210) and 2 μg/mL laminin (Sigma, L2020). Plating medium was completely replaced with growth medium 24 hours after seeding. Plating medium contained MEM (Gibco, 15630080), 10 % horse serum (Gibco, 16050122), 0.6 % D-glucose (Sigma Aldrich, G8769), 0.1

659 % Glutamax (Gibco, 35050061), 2 % penicillin/ 0.1 % streptomycin (Life
660 Technologies,15140122), while growth medium contained Neurobasal (Gibco, 21103049), 3 %
661 B27 (Gibco, 17504044), 0.1 % Glutamax, penicillin/streptomycin 0.1 %). An amount of 100 µL
662 of fresh growth medium was added with a frequency of 48 hours to the somatic compartment to
663 prevent loss of water. Neuronball cell culture was performed as previously reported (Sasaki et al.,
664 2010).Neurons were suspended on growth medium supplemented with 10 % horse serum. A total
665 amount of 30,000 cells was seeded as hanging drops of 20 µL during 3 days inside the cover of
666 100 mm dishes filled with water. Floating spheres were gently washed three times to discard non-
667 attached cells and then seeded on poly-L-lysine coated culture plates. Each well contained 400
668 µL of growth medium previously supplemented with 1 µM cytosine β-D-arabinofuranoside
669 hydrochloride (AraC, Sigma-Aldrich, C1768) to prevent glial growth. Neurites were allowed to
670 grow until 7 days after seeding. The periphery of each neuronballs was carefully scraped with a
671 pipette and washed three times with cold PBS to further remove any remaining cell bodies. Cell-
672 body-containing spheres were extracted by vacuum suction.
673
674 **Immunofluorescence.** Cells were washed twice with PBS and fixed with 4% paraformaldehyde
675 (PFA, Sigma Aldrich, P6148) and 4% sucrose in PBS for 20 min at room temperature. The same
676 procedure was applied to COS-7 cells. For assessment of growth cone morphology, neurons were
677 fixed for 20 min at room temperature by adding an equal volume of 8% PFA and 22% sucrose in
678 PBS directly to the culture medium. After fixation, cells were washed twice with PBS and
679 sequentially incubated for 10 min each at room temperature with: (i) permeabilization solution
680 (0.5% NP-40 [Abcam, ab142227] and 0.5% w/v Bovine Serum Albumin [Winkler, BM-0150] in
681 PBS); (ii) quenching solution (50 mM NH_4Cl in PBS); and (iii) blocking solution (0.5% w/v
682 Bovine Serum Albumin and 5% Fetal Bovine Serum [Sigma Aldrich, F2442] in PBS). Primary
683 antibodies, diluted in 0.5% w/v Bovine Serum Albumin in PBS, were incubated overnight at 4
684 °C. Coverslips were then washed three times (5 min each) with the same solution and incubated
685 with secondary antibodies, diluted in the same buffer, for 1 h at room temperature. Finally,
686 samples were washed with PBS and distilled water and mounted using VECTASHIELD®.
687
688 **Growth cone morphometry.** Growth cones (GCs) were imaged after β3-tubulin and F-actin
689 labeling with phalloidin using identical acquisition settings across conditions. Analyses were
690 performed in FIJI (ImageJ). The actin outline was thresholded (same parameters for all images)
691 to isolate single binarized GCs at distal axon tips (axon shaft excluded). From the binarized GC
692 mask we computed: area (μm^2), perimeter (µm), and elongation ratio (major axis/minor axis of
693 the best-fit ellipse to the actin boundary). For skeleton-based metrics, the binarized GC mask was
694 skeletonized (FIJI Skeletonize) to obtain a one-pixel-wide graph of the actin scaffold. We then
695 used Analyze Skeleton (2D/3D) to extract (i) LSP (Longest Shortest Path), defined as the

maximum geodesic distance (in μm) between any two skeleton nodes within the GC—i.e., the longest of all pairwise shortest paths along the skeleton—and (ii) number of filopodia, defined as the count of terminal branches (end-points in the skeleton) that extend from the GC body and exceed a minimum length of 1.0 μm (same length threshold applied to all conditions). When needed, small spurious branches produced by noise were pruned before counting. All measurements were performed blinded to condition.

Colocalization analysis. COS-7 cells were transfected with indicated plasmids for twenty-four hours and imaged using a confocal microscope (Fluoview FV1000, Olympus) equipped with a UPLSAPO 60×/1.35 NA objective and 4× digital zoom. Images were acquired with a Kalman filter (two iterations). For each condition, an average of 8–12 confocal sections (0.2 μm thickness each) were analyzed per cell. Colocalization between RFP and GFP signals was quantified using Manders' coefficients (M1 and M2) with the JaCoP plugin (Just Another Colocalization Plugin) in ImageJ (FIJI). Identical thresholding parameters were applied to each channel across all conditions.

Fluorescence intensity analysis of COS-7. COS-7 cells were imaged with a Leica TCS SP8 confocal microscope using a 40×/1.30 NA oil-immersion objective. For each field, z-stacks of 15–17 optical sections (1 μm step size) were acquired, and summed intensity projections were generated for analysis. Acquisition parameters (laser power, detector gain, and offset) were kept constant across all conditions. Cells were manually segmented in FIJI using α-tubulin immunostaining to delineate them. For each ROI, mean fluorescence intensity of β3-tubulin, GFP, and RFP channels was measured, and background signal (from a cell-free region of the same image) was subtracted. Corrected mean intensity was multiplied by the cell area to calculate total fluorescence per cell. Fold change values were obtained by normalizing to the mean of the control group.

Fluorescence intensity analysis of somas and axons. Images were acquired using an Olympus BX61WI microscope in wide-field configuration equipped with a 40×/1.30 NA oil-immersion objective and a Hamamatsu ORCA-R2 CCD camera, controlled by Cell^R software (Olympus, Tokyo, Japan). Exposure time, gain, binning, and illumination settings were kept constant across all conditions. For somatic quantifications, cell bodies were manually segmented in FIJI using β3-tubulin staining as a guide, restricting the region of interest (ROI) to the soma and excluding processes. For each cell, the mean background intensity (measured in a cell-free region of the same image) was subtracted from the mean somatic intensity, and total fluorescence (integrated intensity) was calculated by multiplying by the corresponding cell area. Fold change per cell was determined by normalizing to the mean value of the corresponding control group. For axonal

733 quantifications, a 1-µm-wide segmented line was drawn starting at the axon tip and extending 50
734 µm proximally to extract the intensity profile (FIJI). Background intensity was subtracted from
735 each axon profile using values measured in axon-free areas of the same image. For quantifying
736 protein changes, the integrated intensity across the entire 0–50 µm segment was calculated and
737 expressed as fold change relative to controls. To minimize intensity variability across different
738 experimental dates, while preserving the relative differences between conditions, we plotted the
739 corrected intensity profiles. For β3-tubulin, a per-axon baseline was defined by subtracting the
740 intensity at 0 µm (the axon tip) from the entire profile. For Rtn-1, the baseline was defined as the
741 mean pixel intensity within the distal 5 µm of the profile (45–50 µm from the tip), which was
742 subtracted from the entire trace of each axon. These normalizations were applied solely for
743 visualization purposes and were not used in fold change calculations.
744
745 **Stimulated emission depletion (STED) microscopy analysis of axons.** Super-resolution
746 imaging was performed on TCS SP8-3X STED microscope system (Leica Microsystems)
747 equipped with a HC APO CS2 100x/1.40 oil objective. Distal axons of microfluidic chambers
748 were imaged using excitation and depletion laser lines appropriate for each fluorophore (see
749 Reagents in supplementary material). Images were digitized in 1024 × 1024 pixels format file
750 with 5x zoom factor. These settings achieved 18.93 nm resolution in the XY plane and a 220 nm
751 resolution in Z. Four confocal slices from each axon were sum-projected and analyzed. No
752 deconvolution or post-processing algorithms were applied. Instead, all quantitative and qualitative
753 analyses were performed directly on the raw STED images. Acquisition parameters (laser power,
754 detector gain, pixel size, and dwell time) were kept constant across conditions. For quantification,
755 the total fluorescence intensity of the last 15 µm of each distal axon was measured after
756 background subtraction. Two analyses were performed: (i) intensity fold change was calculated
757 by comparing non-axotomized and axotomized axons; and (ii) the relative intensity, which was
758 obtained by dividing the intensity of each pixel by the total intensity of the corresponding staining.
759
760 **Transfections.** All transfections were performed Lipofectamine™ 3000 (Thermo Fisher,
761 L3000001) following manufacturer's instructions but without using p3000 reagent. For neurons
762 and COS-7 cells, RNA or DNA complexes were added to chambers diluted on pure Neurobasal
763 medium. For axonal transfection of siRNAs, medium on the axonal compartment was carefully
764 removed and replaced with 50 µL of the transfection mixture containing 20 pmol of the
765 corresponding oligonucleotide plus 50 µL of fresh growth media. ~300 µL of conditioned medium
766 remained at the somatic compartment, generating positive flux towards the axons. Conversely,
767 for somatic transfection the medium present at the somatic compartment was carefully removed
768 and replaced with 50 µL of the transfection mixture plus 100 µL of fresh growth media, this time
769 generating positive flux towards the soma. For validating siRNA efficiency, 200,000 neurons

770 were seeded on 35 mm plates and transfected with 40 pmol of corresponding oligos and submitted
771 to Western blot after forty-eight hours. For colocalization, Western blot, and immunofluorescence
772 analyses, COS-7 cells were seeded at ~1–2 × 10^5 per 25 mm coverslip and cultured for 24 h before
773 transfection with 500 ng of pCMV3-C-GFPSpark plasmid encoding either Rtn-1C-GFP or Rtn-
774 1A-GFP, together with pCMV3-C-ORFSpark encoding Spastin-RFP (all plasmids are detailed in
775 the Reagents section of the Supplementary material).
776
777 **Axotomy and Sholl analysis.** At 8 DIV, axons were removed from the axonal compartment of
778 microfluidic chambers by vacuum aspiration performed five times with 100 µL of pure
779 Neurobasal medium. Subsequently, all media was removed, and the transfection mixture was
780 added either to the axonal or somatic compartment. For quantification of axonal outgrowth, β3-
781 tubulin–stained axons were identically thresholded across conditions, binarized, and curated to
782 fully trace axonal trajectories. The Sholl analysis was performed in FIJI using the NeuroAnatomy
783 plugin. Concentric semi-circles were applied at 2 µm radial intervals, starting from the ends of
784 the microgrooves and centered on axonal fields of equivalent size. The analysis extended to a
785 maximum radial distance of either 1200 µm or 1500 µm, depending on the experiment.
786
787 **Probe-labeling of primary antibodies for puromycylation proximity ligation assay (puro-**
788 **PLA).** Monoclonal antibodies mouse anti-Reticulon-1C and mouse anti-puromycin (3RH1,
789 Kerafast) were directly labeled with the Duolink® In Situ Probemaker™ PLUS (1002748995,
790 Sigma Aldrich) and MINUS (1002748992, Sigma Aldrich), respectively, following
791 manufacturer's instructions. Both antibodies with a concentration of 1 µg/µL were labeled
792 overnight at room temperature with the corresponding buffer and probes to a final volume of 20
793 µL. Labeled antibodies were further diluted with 20 µL of storage solution.
794
795 **Puro-PLA staining protocol.** Puro-PLA was under conditions similar to well-established
796 protocols (Dieck et al., 2015). Briefly, a 15-min pulse of 1.8 µM puromycin (P8833, Sigma-
797 Aldrich) was applied exclusively to the axonal or somatic compartment of microfluidic chambers
798 containing 9 DIV cortical neurons. As an additional control, this incubation was performed after
799 90 min of local pretreatment with 40 nM emetine (E2375, Sigma-Aldrich) in distilled water
800 (vehicle), added either to the somatic or axonal compartment to block protein synthesis.
801 Immediately after incubations, cells were washed twice with PBS and fixed with 4% PFA and
802 4% sucrose in PBS for 20 min at room temperature, followed by three PBS washes (5 min each).
803 Cells were then permeabilized with 0.25% Triton X-100 in PBS for 10 min, washed three times
804 with PBS (5 min each), blocked with 5% goat serum in PBS for 1 h, and incubated overnight at 4
805 °C with probe-labeled antibodies (anti–Reticulon-1C, 1:50; anti-puromycin, 1:200) diluted in the
806 same blocking solution. Detection of locally synthesized Reticulon-1C was performed following

807 the manufacturer's instructions, except that no labeled secondary antibody step was included.
808 Afterward, cells were incubated for 1 h at room temperature with anti-β3-tubulin conjugated to
809 Alexa Fluor 488 and mounted with Duolink® In Situ Mounting Medium with DAPI (Sigma-
810 Aldrich). Images were acquired as previously described using a Zeiss LSM 800 confocal
811 microscope with a 63× oil objective. PLA-positive puncta present within a β3-tubulin mask that
812 defined the axonal area were quantified using FIJI software.
813
814 **RT-PCR from neuronballs and microfluidic chambers.** For axonal RNA isolation from
815 neuronballs, at least 200 balls were desomatized and processed with RNAqueous™-Micro Total
816 RNA Isolation Kit (AM193, Thermo Fisher), following the manufacturer's instructions.
817 Approximately 20–30 axotomized neuronballs (somatic RNA) were processed using the same
818 protocol. Reverse transcription was performed from 100 ng of RNA as input using the High-
819 Capacity cDNA Reverse Transcription Kit (4368814, Thermo Fisher). For negative controls,
820 axonal samples were submitted to the same protocol, but without adding reverse transcriptase.
821 Resulting cDNA products were treated with DNase according to the manufacturer's instructions
822 (EN0521, Thermo Fisher). For PCR, cDNA was amplified using the GoTaq® Green Master Mix,
823 2X (M712, Promega), with the following cycling parameters: initial denaturation at 95 °C for 5
824 min; 35 cycles of denaturation at 95 °C for 30 s, annealing at 57 °C for 30 s, and extension at 72
825 °C for 45 s; followed by a final extension at 72 °C for 10 min. PCR products were loaded on a
826 2% agarose gel and stained with GelRed® Nucleic Acid Gel Stain (Biotium, 41003), following
827 the manufacturer's recommendations. We performed the RNA isolation from the axonal/somatic
828 compartments of microfluidic chambers (7-8 chambers) as previously reported (Taylor et al.,
829 2005).For the subsequent steps, we followed the same procedures as in neuronballs, but
830 performing 42 PCR cycles.
831
832 **Western blot.** Proteins were isolated using RIPA buffer (50 mM Tris-HCl, pH 7.4, 150 mM
833 NaCl, 0.25% sodium deoxycholate, 1% NP-40, 1% SDS, 1 mM EDTA) supplemented with
834 protease and phosphatase inhibitors (Thermo Fisher, A32963). Extracted proteins were quantified
835 using the Bicinchoninic Acid (BCA) method (Thermo Fisher, 23225) and separated on
836 polyacrylamide gels under denaturing conditions (SDS-PAGE; Cleveland et al., 1977). For each
837 sample, 20 µg of protein was loaded per lane for both complete neuronal or cell homogenates,
838 and axonal or somatic fractions of neuronballs. Proteins were resolved on 15% acrylamide gels
839 by electrophoresis at 70 V for 45 min followed by 100 V for 45 min. Gels were transferred to
840 nitrocellulose membranes (Bio-Rad) at a constant current of 350 mA for 90 min. After transfer,
841 membranes were blocked with 5% (w/v) skim milk in PBS for one hour at room temperature
842 under constant agitation and then incubated overnight at 4 °C with the corresponding primary
843 antibody diluted in PBS. Membranes were incubated with the appropriate secondary antibody for

844 one hour at room temperature. When indicated, total protein loading was normalized using No-
845 Stain™ total protein labeling reagent (Thermo Fisher, A44449) according to the manufacturer's
846 instructions. Bands and lanes were quantified by densitometry using Photoshop 7.0 (Adobe).
847
848 **Live imaging of microtubule plus-ends.** Cortical neurons were cultured in microfluidic
849 chambers and transfected with EB3-Emerald GFP plasmid at 7 DIV. At 8 DIV, neurons were
850 axotomized by vacuum aspiration, and siRNAs were transfected into the axonal compartment
851 .The Spastin inhibitor Spastazoline (HY-111548, MedChemExpress) was added to the axonal
852 compartment 4–5 h after axotomy at a final concentration of 50 nM. Forty-four hours after
853 transfection, axons expressing EB3-GFP were randomly selected and imaged in Tyrode's solution
854 (125 mM NaCl, 2 mM KCl, 2 mM $CaCl_2$, 2 mM $MgCl_2$, 30 mM glucose, 25 mM HEPES, pH 7.4)
855 at 32 °C. Cells were equilibrated for 10 min before recording. Movies were acquired for 3 min at
856 2 frames per second (fps). To maintain hydrostatic pressure towards the axonal side, the volume
857 difference between compartments was carefully preserved throughout the experiment. Imaging
858 was performed on an inverted microscope (Observer.D1, Zeiss) equipped with an EMCCD
859 camera (Evolve 512, Photometrics) controlled by VisiView® software (Visitron Systems GmbH).
860 A 63× oil-immersion objective and a GFP single-band exciter ET filter set (excitation 470/40,
861 emission 59022m, dichroic 59022BS) were used. The mEmerald-EB3-C-20 plasmid was a gift
862 from Michael Davidson (Addgene plasmid #54076; http://n2t.net/addgene:54076; RRID:
863 Addgene_54076).
864
865 **Analysis of microtubule dynamics.** All acquired time series were filtered using the Gaussian
866 Blur in FIJI (applied to temporal frames). Mobile components of the series were isolated by
867 applying a 4-sigma Gaussian blur, while static elements were extracted by applying a 50-sigma
868 blur. To enhance detection of moving structures, static components were subtracted from mobile
869 components using the *Image Calculator* function in FIJI. The resulting filtered image series were
870 then used to generate kymographs with the FIJI plugin *Kymograph Builder*. Kymographs were
871 constructed from the distal portion of axons by tracing a 1-µm-wide line, with a total length
872 ranging from 30 to 50 µm. Growth cones were excluded from the analysis. All analyzed
873 parameters were quantified as previously described (Stepanova et al., 2010). EB3-GFP comets
874 were analyzed from kymographs in FIJI. Individual dashes corresponding to microtubule growth
875 events were manually traced using the Segmented Line tool. The angle of each dash was measured
876 relative to the x-axis. The horizontal projection of the dash, obtained by multiplying its length by
877 the cosine of the angle, represents the distance traveled by the comet in micrometers (track
878 length). The vertical projection, obtained by multiplying the dash length by the sine of the angle,
879 was proportional to comet lifetime. To obtain comet lifetime in seconds, vertical projection was
880 divided by the total y-axis length of the recording kymograph and multiplied by the total

881 acquisition time (180 seconds for a 3-minute movie). Growth rate was calculated by dividing the
882 track length by the comet lifetime for each dash.
883
884 **Molecular docking between Spastin (M87) and Rtn-1C**. First, Spastin M87 and Rtn-1A models
885 of *Rattus norvegicus* were retrieved from AlphaFold Protein Structure Database (accession
886 numbers AF-A0A0G2K590 and AF-Q64548, respectively). Then, M87 spastin model were
887 generated from the removal of the first 86 amino acids of the M1 Spastin model, whereas Rtn-1C
888 3D-structure was built with MODELLER version 10.4 using an Rtn-1A model as template. For
889 this, amino acid sequences of Rtn-1C were retrieved from UniProtKB/Swiss-Prot (accession
890 numbers Q64548). Additionally, the first 20 amino acids (of the N-terminal region) of the Rtn-
891 1C model and region 200-317 containing the microtubule-binding domain of Spastin M87 were
892 refined using ModLoop server (Fiser & Sali, 2003). Subsequently, we evaluated the interaction
893 of the Rtn-1C N-terminal with three domains of Spastin M87- endosome or MIT (region 116-
894 194), microtubule-binding (region 270-328) and microtubule-severing o AAA ATPase (region
895 342-599) - using the HADDOCK docking protein-protein web server(Van Zundert et al., 2016).
896 Among many models, low-energy conformations for each complex were extracted from
897 HADDOCK 2.2 server, as previously described (Acevedo et al., 2018) The binding energy
898 (ΔG_bind) of the complexes were predicted using the PRODIGY web server at a temperature of
899 310 K, and chain identifiers for Rtn-1 and Spastin M87 were specified as Interactor 1 and 2,
900 respectively. Finally, graphical analysis of molecular docking studies was performed using VMD
901 1.9.2 software(Humphrey et al., 1996) .
902
903 **Statistical Analysis.** Unless otherwise stated, data are presented as mean ± standard error.
904 Normality was assessed using the Shapiro–Wilk test. For normally distributed data, comparisons
905 between two groups were performed using two-tailed Student's t-test; for non-normally
906 distributed data, the two-tailed Mann–Whitney *U t*est was applied. Western blot fold change
907 values were compared to a theoretical mean of 1 using the Wilcoxon signed-rank test. For
908 comparisons among multiple groups, one-way ANOVA followed by Tukey's post hoc test was
909 used for normally distributed data, whereas the Kruskal–Wallis test followed by Dunn's post hoc
910 test was applied for non-parametric data. Statistical significance was defined as $p < 0.05$.
911 Fluorescence intensity experiments in Figures 2 and 4 were analyzed at the single-cell level using
912 linear mixed-effects (LME) models, with experimental date included as a random effect.
913 Statistical tests were performed using GraphPad Prism (GraphPad Software, San Diego, CA,
914 USA) and R (v4.0 or later) with the lme4 and lmerTest packages.

References

Acevedo, W., Ramírez-Sarmiento, C. A., & Agosin, E. (2018). Identifying the interactions between natural, non-caloric sweeteners and the human sweet receptor by molecular docking. *Food Chemistry*, *264*, 164–171. https://doi.org/10.1016/J.FOODCHEM.2018.04.113

Aiken, J., & Holzbaur, E. L. F. (2024). Spastin locally amplifies microtubule dynamics to pattern the axon for presynaptic cargo delivery. *BioRxiv*, *123*(3), 332a. https://doi.org/10.1101/2023.08.08.552320

Allison, R., Edgar, J. R., & Reid, E. (2019). Spastin MIT Domain Disease-Associated Mutations Disrupt Lysosomal Function. *Frontiers in Neuroscience*, *13*, 486039. https://doi.org/10.3389/FNINS.2019.01179/BIBTEX

Allison, R., Lumb, J. H., Fassier, C., Connell, J. W., Martin, D. Ten, Seaman, M. N. J., Hazan, J., & Reid, E. (2013). An ESCRT-spastin interaction promotes fission of recycling tubules from the endosome. *Journal of Cell Biology*, *202*(3), 527–543. https://doi.org/10.1083/JCB.201211045/VIDEO-2

Aridor, M., & Fish, K. N. (2009). Selective Targeting of ER Exit Sites Supports Axon Development. *Traffic*, *10*(11), 1669–1684. https://doi.org/10.1111/j.1600-0854.2009.00974.x

Baas, P. W., Rao, A. N., Matamoros, A. J., & Leo, L. (2016). Stability properties of neuronal microtubules. *Cytoskeleton (Hoboken, N.J.)*, *73*(9), 442. https://doi.org/10.1002/CM.21286

Baleriola, J., Walker, C. A., Jean, Y. Y., Crary, J. F., Troy, C. M., Nagy, P. L., & Hengst, U. (2014). Axonally synthesized ATF4 transmits a neurodegenerative signal across brain regions. *Cell*, *158*(5), 1159–1172. https://doi.org/10.1016/J.CELL.2014.07.001

Batista, A. F. R., Martínez, J. C., & Hengst, U. (2017). Intra-axonal Synthesis of SNAP25 Is Required for the Formation of Presynaptic Terminals. *Cell Reports*. https://doi.org/10.1016/j.celrep.2017.08.097

Bigler, R. L., Kamande, J. W., Dumitru, R., Niedringhaus, M., & Taylor, A. M. (2017). Messenger RNAs localized to distal projections of human stem cell derived neurons. *Scientific Reports 2017 7:1*, *7*(1), 1–11. https://doi.org/10.1038/s41598-017-00676-w

Blackstone, C., Kane, C. J. O., Reid, E., O'Kane, C. J., & Reid, E. (2011). Hereditary spastic paraplegias: membrane traffic and the motor pathway. *Nature Reviews. Neuroscience*, *12*(1), 31–42. https://doi.org/10.1038/nrn2946

Brizuela, M., Blizzard, C. A., Chuckowree, J. A., Dawkins, E., Gasperini, R. J., Young, K. M., & Dickson, T. C. (2015). The microtubule-stabilizing drug Epothilone D increases axonal sprouting following transection injury in vitro. *Molecular and Cellular Neuroscience*, *66*(PB), 129–140. https://doi.org/10.1016/j.mcn.2015.02.006

Chiurchiù, V., Maccarrone, M., & Orlacchio, A. (2014). The role of reticulons in neurodegenerative diseases. *Neuromolecular Medicine*, *16*(1), 3–15. https://doi.org/10.1007/s12017-013-8271-9

Cooke, P., Janowitz, H., & Dougherty, S. E. (2022). Neuronal Redevelopment and the Regeneration of Neuromodulatory Axons in the Adult Mammalian Central Nervous System. *Frontiers in Cellular Neuroscience*, *16*, 872501. https://doi.org/10.3389/FNCEL.2022.872501/BIBTEX

Cornejo, V. H., Luarte, A., & Couve, A. (2017). Global and local mechanisms sustain axonal proteostasis of transmembrane proteins. *Traffic*, *18*(5), 255–266. https://doi.org/10.1111/tra.12472

Cupido, T., Pisa, R., Kelley, M. E., & Kapoor, T. M. (2019). Designing a chemical inhibitor of the AAA protein spastin using active site mutations. *Nature Chemical Biology*, *15*(5), 444. https://doi.org/10.1038/S41589-019-0225-6

D' Eletto, M., Risuglia, A., Oliverio, S., Mehdawy, B., Nardacci, R., Bordi, M., & Di Sano, F. (2019). Modulation of autophagy by RTN-1C: role in autophagosome biogenesis. *Cell Death & Disease*, *10*(12). https://doi.org/10.1038/S41419-019-2099-7

de Juan-Sanz, J., Holt, G. T., Schreiter, E. R., de Juan, F., Kim, D. S., & Ryan, T. A. (2017). Axonal Endoplasmic Reticulum Ca2+ Content Controls Release Probability in CNS Nerve Terminals. *Neuron*, *93*(4), 867-881.e6. https://doi.org/10.1016/J.NEURON.2017.01.010

Deitch, J. S., & Banker, G. A. (1993). An electron microscopic analysis of hippocampal neurons developing in culture: early stages in the emergence of polarity. *The Journal of Neuroscience : The Official Journal of the Society for Neuroscience*, *13*(10), 4301–4315. https://doi.org/10.1523/jneurosci.1544-09.2009

Dieck, S. tom, Kochen, L., Hanus, C., Bartnik, I., Nassim-Assir, B., Merk, K., Mosler, T., Garg, S., Bunse, S., Tirrell, D. A., & Schuman, E. M. (2015). Direct visualization of identified and newly synthesized proteins in situ. *Nature Methods*. https://doi.org/10.1038/nmeth.3319

Evans, K., Keller, C., Pavur, K., Glasgow, K., Conn, B., & Lauring, B. (2006). Interaction of two hereditary spastic paraplegia gene products, spastin and atlastin, suggests a common pathway for axonal maintenance. *Proceedings of the National Academy of Sciences of the United States of America*. https://doi.org/10.1073/pnas.0510863103

Fan, X. xuan, Hao, Y. ying, Guo, S. wen, Zhao, X. ping, Xiang, Y., Feng, F. xue, Liang, G. ting, & Dong, Y. wei. (2018). Knockdown of RTN1-C attenuates traumatic neuronal injury through regulating intracellular Ca2+ homeostasis. *Neurochemistry International*, *121*, 19–25. https://doi.org/10.1016/J.NEUINT.2018.10.018

Farías, G. G., Fréal, A., Tortosa, E., Stucchi, R., Pan, X., Portegies, S., Will, L., Altelaar, M., & Hoogenraad, C. C. (2019). Feedback-Driven Mechanisms between Microtubules and the Endoplasmic Reticulum Instruct Neuronal Polarity. *Neuron*. https://doi.org/10.1016/j.neuron.2019.01.030

Farias, J., Holt, C. E., Sotelo, J. R., & Sotelo-Silveira, J. R. (2020). Axon microdissection and transcriptome profiling reveals the in vivo RNA content of fully differentiated myelinated motor axons. *RNA (New York, N.Y.)*, *26*(5), 595–612. https://doi.org/10.1261/RNA.073700.119

González, C., Cánovas, J., Fresno, J., Couve, E., Court, F. A., & Couve, A. (2016). Axons provide the secretory machinery for trafficking of voltage-gated sodium channels in peripheral nerve. *Proceedings of the National Academy of Sciences of the United States of America*, *113*(7), 1823–1828. https://doi.org/10.1073/PNAS.1514943113

Gumy, L. F., Yeo, G. S. H., Tung, Y. C. L., Zivraj, K. H., Willis, D., Coppola, G., Lam, B. Y. H., Twiss, J. L., Holt, C. E., & Fawcett, J. W. (2011). Transcriptome analysis of embryonic and adult sensory axons reveals changes in mRNA repertoire localization. *RNA (New York, N.Y.)*, *17*(1), 85–98. https://doi.org/10.1261/RNA.2386111

Hazan, J., Fonknechten, N., Mavel, D., Paternotte, C., Samson, D., Artiguenave, F., Davoine, C.-S., Cruaud, C., Dürr, A., Wincker, P., Brottier, P., Cattolico, L., Barbe, V., Burgunder, J.-M., Prud'homme, J.-F., Brice, A., Fontaine, B., Heilig, R., & Weissenbach, J. (1999). Spastin, a new AAA protein, is altered in the most frequent form of autosomal dominant spastic paraplegia. *Nature Genetics*, *23*(3), 296–303. https://doi.org/10.1038/15472

He, Z., & Jin, Y. (2016). Intrinsic Control of Axon Regeneration. *Neuron*, *90*(3), 437–451. https://doi.org/10.1016/J.NEURON.2016.04.022

Humphrey, W., Dalke, A., & Schulten, K. (1996). VMD: Visual molecular dynamics. *Journal of Molecular Graphics*, *14*(1), 33–38. https://doi.org/10.1016/0263-7855(96)00018-5

Iwahashi, J., Hamada, N., & Watanabe, H. (2007). Two hydrophobic segments of the RTN1 family determine the ER localization and retention. *Biochemical and Biophysical Research Communications*, *355*(2), 508–512. https://doi.org/10.1016/j.bbrc.2007.02.001

Jin, L. Q., Zhou, Y., Li, Y. S., Zhang, G., Hu, J., & Selzer, M. E. (2022). Transcriptomes of Injured Lamprey Axon Tips: Single-Cell RNA-Seq Suggests Differential Involvement of MAPK Signaling Pathways in Axon Retraction and Regeneration after Spinal Cord Injury. *Cells*, *11*(15), 2320. https://doi.org/10.3390/CELLS11152320/S1

Jung, H., Gkogkas, C. G., Sonenberg, N., & Holt, C. E. (2014). Remote control of gene function by local translation. In *Cell*. https://doi.org/10.1016/j.cell.2014.03.005

Kaethner, R. J., & Stuermer, C. A. 0. (1992). Dynamics of Terminal Arbor Formation and Target Approach of Retinotectal Axons in Living Zebrafish Embryos: A Time-Lapse Study of Single Axons. *The Journal of Neuroscience*, *72*(8), 32573271.

Kaya, L., Meissner, B., Riedl, M. C., Muik, M., Schwarzer, C., Ferraguti, F., Sarg, B., Lindner, H., Schweigreiter, R., Knaus, H. G., Romanin, C., & Bandtlow, C. E. (2013). Direct association of the reticulon protein RTN1A with the ryanodine receptor 2 in neurons. *Biochimica et Biophysica Acta*, *1833*(6), 1421. https://doi.org/10.1016/J.BBAMCR.2013.02.012

Kiss, A., Fischer, I., Kleele, T., Misgeld, T., & Propst, F. (2018). Neuronal growth cone size-dependent and -independent parameters of microtubule polymerization. *Frontiers in Cellular Neuroscience*, *12*, 195. https://doi.org/10.3389/FNCEL.2018.00195/FULL

Koppers, M., Özkan, N., Nguyen, H. H., Jurriens, D., McCaughey, J., Nguyen, D. T. M., Li, C. H., Stucchi, R., Altelaar, M., MacGillavry, H. D., Kapitein, L. C., Hoogenraad, C. C., & Farías, G. G. (2024). Axonal endoplasmic reticulum tubules control local translation via P180/RRBP1-mediated ribosome interactions. *Developmental Cell*, *0*(0). https://doi.org/10.1016/j.devcel.2024.05.005

Krijnse-Locker, J., Parton, R. G., Fuller, S. D., Griffiths, G., & Dotti, C. G. (1995). The organization of the endoplasmic reticulum and the intermediate compartment in cultured rat hippocampal neurons. *Molecular Biology of the Cell*, *6*(10), 1315–1332. https://doi.org/10.1091/mbc.6.10.1315

Kuo, Y. W., & Howard, J. (2021). Cutting, Amplifying, and Aligning Microtubules with Severing Enzymes. *Trends in Cell Biology*, *31*(1), 50. https://doi.org/10.1016/J.TCB.2020.10.004

Kuo, Y. W., Trottier, O., Mahamdeh, M., & Howard, J. (2019). Spastin is a dual-function enzyme that severs microtubules and promotes their regrowth to increase the number and mass of microtubules. *Proceedings of the National Academy of Sciences of the United States of America*, *116*(12), 5533–5541. https://doi.org/10.1073/PNAS.1818824116/SUPPL_FILE/PNAS.1818824116.SM03.AVI

Lee, M., Paik, S. K., Lee, M. J., Kim, Y. J., Kim, S., Nahm, M., Oh, S. J., Kim, H. M., Yim, J., Lee, C. J., Bae, Y. C., & Lee, S. (2009). Drosophila Atlastin regulates the stability of muscle microtubules and is required for synapse development. *Developmental Biology*, *330*(2), 250–262. https://doi.org/10.1016/J.YDBIO.2009.03.019

Lin, H.-M., Kuang, J.-X., Sun, P., Li, N., Lv, X., & Zhang, Y.-H. (2018). Reconstruction of Intratelencephalic Neurons in the Mouse Secondary Motor Cortex Reveals the Diverse Projection Patterns of Single Neurons. *Frontiers in Neuroanatomy*, *12*. https://doi.org/10.3389/fnana.2018.00086

Lin, Y. F., Xie, Z., Zhou, J., Chen, H. H., Shao, W. W., & Lin, H. D. (2019). Effect of exogenous spastin combined with polyethylene glycol on sciatic nerve injury. *Neural Regeneration Research*, *14*(7), 1271–1279. https://doi.org/10.4103/1673-5374.251336

Liu, B., Liu, S., & Sun, D. (2023). Low-Dose Taxol Promotes Neuronal Axons Extension and Functional Recovery after Spinal Cord Injury. *Mediators of Inflammation*, *2023*, 5604103. https://doi.org/10.1155/2023/5604103

Liu, Q., Yang, H., Luo, J., Peng, C., Wang, K., Zhang, G., Lin, H., & Ji, Z. (2024). 14-3-3 protein augments the protein stability of phosphorylated spastin and promotes the recovery of spinal cord injury through its agonist intervention. *ELife*, *12*. https://doi.org/10.7554/eLife.90184

Liz, M. A., Mar, F. M., Santos, T. E., Pimentel, H. I., Marques, A. M., Morgado, M. M., Vieira, S., Sousa, V. F., Pemble, H., Wittmann, T., Sutherland, C., Woodgett, J. R., & Sousa, M. M. (2014). Neuronal deletion of GSK3β increases microtubule speed in the growth cone and enhances axon regeneration via CRMP-2 and independently of MAP1B and CLASP2. *BMC Biology*, *12*(1), 1–19. https://doi.org/10.1186/1741-7007-12-47/FIGURES/8

Lopez-Verrilli, M. A., Picou, F., & Court, F. A. (2013). Schwann cell-derived exosomes enhance axonal regeneration in the peripheral nervous system. *GLIA*. https://doi.org/10.1002/glia.22558

Luarte, A., Cornejo, V. H., Bertin, F., Gallardo, J., & Couve, A. (2018). The axonal endoplasmic reticulum: One organelle—many functions in development, maintenance, and plasticity. In *Developmental Neurobiology*. https://doi.org/10.1002/dneu.22560

Maciel, R., Bis, D. M., Rebelo, A. P., Saghira, C., Züchner, S., & Saporta, M. A. (2018). The human motor neuron axonal transcriptome is enriched for transcripts related to mitochondrial function and microtubule-based axonal transport. *Experimental Neurology*, *307*, 155. https://doi.org/10.1016/J.EXPNEUROL.2018.06.008

Mannan, A. U., Boehm, J., Sauter, S. M., Rauber, A., Byrne, P. C., Neesen, J., & Engel, W. (2006). Spastin, the most commonly mutated protein in hereditary spastic paraplegia interacts with Reticulon 1 an endoplasmic reticulum protein. *Neurogenetics*, *7*(2), 93–103. https://doi.org/10.1007/s10048-006-0034-4

Matamoros, A. J., Tom, V. J., Wu, D., Rao, Y., Sharp, D. J., & Baas, P. W. (2019). Knockdown of Fidgetin Improves Regeneration of Injured Axons by a Microtubule-Based Mechanism. *Journal of Neuroscience*, *39*(11), 2011–2024. https://doi.org/10.1523/JNEUROSCI.1888-18.2018

McCurdy, E. P., Chung, K. M., Benitez-Agosto, C. R., & Hengst, U. (2019). Promotion of Axon Growth by the Secreted End of a Transcription Factor. *Cell Reports*, *29*(2), 363. https://doi.org/10.1016/J.CELREP.2019.08.101

Nepravishta, R., Bellomaria, A., Polizio, F., Paci, M., & Melino, S. (2010). Reticulon RTN1-CCT peptide: A potential nuclease and inhibitor of histone deacetylase enzymes. *Biochemistry*, *49*(2), 252–258. https://doi.org/10.1021/BI9012676/SUPPL_FILE/BI9012676_SI_001.PDF

Nepravishta, R., Polizio, F., Paci, M., & Melino, S. (2012). A metal-binding site in the RTN1-C protein: new perspectives on the physiological role of a neuronal protein. *Metallomics*, *4*(5), 480–487. https://doi.org/10.1039/C2MT20035J

Nijssen, J., Aguila, J., Hoogstraaten, R., Kee, N., & Hedlund, E. (2018). Axon-Seq Decodes the Motor Axon Transcriptome and Its Modulation in Response to ALS. *Stem Cell Reports*, *11*(6), 1565. https://doi.org/10.1016/J.STEMCR.2018.11.005

Nozumi, M., Togano, T., Takahashi-Niki, K., Lu, J., Honda, A., Taoka, M., Shinkawa, T., Koga, H., Takeuchi, K., Isobe, T., & Igarashi, M. (2009). Identification of functional marker proteins in the mammalian growth cone. *Proceedings of the National Academy of Sciences of the United States of America*, *106*(40), 17211–17216. https://doi.org/10.1073/pnas.0904092106

Pacheco, A., Merianda, T. T., Twiss, J. L., & Gallo, G. (2020). Mechanism and role of the intra-axonal Calreticulin translation in response to axonal injury. *Experimental Neurology*. https://doi.org/10.1016/j.expneurol.2019.113072

Pavez, M., Thompson, A. C., Arnott, H. J., Mitchell, C. B., D'Atri, I., Don, E. K., Chilton, J. K., Scott, E. K., Lin, J. Y., Young, K. M., Gasperini, R. J., & Foa, L. (2019). STIM1 is required for remodeling of the endoplasmic reticulum and microtubule cytoskeleton in steering growth cones. *Journal of Neuroscience*. https://doi.org/10.1523/JNEUROSCI.2496-18.2019

Petrova, V., Pearson, C. S., Ching, J., Tribble, J. R., Solano, A. G., Yang, Y., Love, F. M., Watt, R. J., Osborne, A., Reid, E., Williams, P. A., Martin, K. R., Geller, H. M., Eva, R., & Fawcett, J. W. (2020). Protrudin functions from the endoplasmic reticulum to support axon regeneration in the adult CNS. *Nature Communications 2020 11:1*, *11*(1), 1–15. https://doi.org/10.1038/s41467-020-19436-y

Rao, K., Stone, M. C., Weiner, A. T., Gheres, K. W., Zhou, C., Deitcher, D. L., Levitan, E. S., & Rolls, M. M. (2016). Spastin, atlastin, and ER relocalization are involved in axon but not dendrite regeneration. *Molecular Biology of the Cell*. https://doi.org/10.1091/mbc.E16-05-0287

Reali, V., Mehdawy, B., Nardacci, R., Filomeni, G., Risuglia, A., Rossin, F., Antonioli, M., Marsella, C., Fimia, G. M., Piacentini, M., & Di Sano, F. (2015). Reticulon protein-1C is a key component of MAMs. *Biochimica et Biophysica Acta*, *1853*(3), 733–745. https://doi.org/10.1016/J.BBAMCR.2014.12.031

Roebroek, A. J. M., Van De Velde, H. J. K., Van Bokhoven, A., Broers, J. L. V, Ramaekers, F. C. S., & Van De Ven, W. J. M. (1993). Cloning and expression of alternative transcripts of a novel neuroendocrine-specific gene and identification of its 135-kDa translational product. *Journal of Biological Chemistry*, *268*(18), 13439–13447.

Roll-Mecak, A., & Vale, R. D. (2008). Structural basis of microtubule severing by the hereditary spastic paraplegia protein spastin. *Nature*. https://doi.org/10.1038/nature06482

Rolls, M. M., Thyagarajan, P., & Feng, C. (2020). Microtubule dynamics in healthy and injured neurons. *Developmental Neurobiology*, *81*(3), 321. https://doi.org/10.1002/DNEU.22746

Rotem, N., Magen, I., Ionescu, A., Gershoni-Emek, N., Altman, T., Costa, C. J., Gradus, T., Pasmanik-Chor, M., Willis, D. E., Ben-Dov, I. Z., Hornstein, E., & Perlson, E. (2017). ALS Along the Axons - Expression of Coding and Noncoding RNA Differs in Axons of ALS models. *Scientific Reports*, *7*. https://doi.org/10.1038/SREP44500

Saal, L., Briese, M., Kneitz, S., Glinka, M., & Sendtner, M. (2014). Subcellular transcriptome alterations in a cell culture model of spinal muscular atrophy point to widespread defects in axonal growth and presynaptic differentiation. *RNA (New York, N.Y.)*, *20*(11), 1789–1802. https://doi.org/10.1261/RNA.047373.114

Sahu, R., Kaushik, S., Clement, C. C., Cannizzo, E. S., Scharf, B., Follenzi, A., Potolicchio, I., Nieves, E., Cuervo, A. M., & Santambrogio, L. (2011). Microautophagy of Cytosolic Proteins by Late Endosomes. *Developmental Cell*, *20*(1), 131–139. https://doi.org/10.1016/J.DEVCEL.2010.12.003

Sasaki, Y., Welshhans, K., Wen, Z., Yao, J., Xu, M., Goshima, Y., Zheng, J. Q., & Bassell, G. J. (2010). Phosphorylation of Zipcode Binding Protein 1 Is Required for Brain-Derived Neurotrophic Factor Signaling of Local -Actin Synthesis and Growth Cone Turning. *Journal of Neuroscience*, *30*(28), 9349–9358. https://doi.org/10.1523/JNEUROSCI.0499-10.2010

Sengottuvel, V., Leibinger, M., Pfreimer, M., Andreadaki, A., & Fischer, D. (2011). Taxol Facilitates Axon Regeneration in the Mature CNS. *Journal of Neuroscience*, *31*(7), 2688–2699. https://doi.org/10.1523/JNEUROSCI.4885-10.2011

Shigeoka, T., Jung, H., Jung, J., Turner-Bridger, B., Ohk, J., Lin, J. Q., Amieux, P. S., & Holt, C. E. (2016). Dynamic Axonal Translation in Developing and Mature Visual Circuits. *Cell*, *166*(1), 181–192. https://doi.org/10.1016/j.cell.2016.05.029

Shigeoka, T., Koppers, M., Wong, H. H. W., Lin, J. Q., Cagnetta, R., Dwivedy, A., de Freitas Nascimento, J., van Tartwijk, F. W., Ströhl, F., Cioni, J. M., Schaeffer, J., Carrington, M., Kaminski, C. F., Jung, H., Harris, W. A., & Holt, C. E. (2019). On-Site Ribosome Remodeling by Locally Synthesized Ribosomal Proteins in Axons. *Cell Reports*, *29*(11), 3605-3619.e10. https://doi.org/10.1016/j.celrep.2019.11.025

Sholl, D. A. (1953). Dendritic organization in the neurons of the visual and motor cortices of the cat. *Journal of Anatomy*, *87*(Pt 4), 387. https://pmc.ncbi.nlm.nih.gov/articles/PMC1244622/

Solowska, J. M., Rao, A. N., & Baas, P. W. (2017). Truncating mutations of SPAST associated with hereditary spastic paraplegia indicate greater accumulation and toxicity of the M1 isoform of spastin. *Molecular Biology of the Cell*, *28*(13), 1728. https://doi.org/10.1091/MBC.E17-01-0047

Song, W., Cho, Y., Watt, D., & Cavalli, V. (2015). Tubulin-tyrosine ligase (TTL)-mediated increase in tyrosinated α-tubulin in injured axons is required for retrograde injury signaling and axon regeneration. *Journal of Biological Chemistry*, *290*(23), 14765–14775. https://doi.org/10.1074/jbc.M114.622753

Stepanova, T., Slemmer, J., Hoogenraad, C. C., Lansbergen, G., Dortland, B., De Zeeuw, C. I., Grosveld, F., Van Cappellen, G., Akhmanova, A., & Galjart, N. (2003). Visualization of Microtubule Growth in Cultured Neurons via the Use of EB3-GFP (End-Binding Protein 3-Green Fluorescent Protein). *Journal of Neuroscience*, *23*(7), 2655–2664. https://doi.org/10.1523/JNEUROSCI.23-07-02655.2003

Stepanova, T., Smal, I., Van Haren, J., Akinci, U., Liu, Z., Miedema, M., Limpens, R., Van Ham, M., Van Der Reijden, M., Poot, R., Grosveld, F., Mommaas, M., Meijering, E., & Galjart,

N. (2010). History-dependent catastrophes regulate axonal microtubule behavior. *Current Biology*. https://doi.org/10.1016/j.cub.2010.04.024

Stone, M. C., Rao, K., Gheres, K. W., Kim, S., Tao, J., La Rochelle, C., Folker, C. T., Sherwood, N. T., & Rolls, M. M. (2012). Normal Spastin Gene Dosage Is Specifically Required for Axon Regeneration. *Cell Reports*, *2*(5), 1340–1350. https://doi.org/10.1016/j.celrep.2012.09.032

Taylor, A. M., Berchtold, N. C., Perreau, V. M., Tu, C. H., Li Jeon, N., & Cotman, C. W. (2009). Axonal mRNA in Uninjured and Regenerating Cortical Mammalian Axons. *Journal of Neuroscience*, *29*(15), 4697–4707. https://doi.org/10.1523/JNEUROSCI.6130-08.2009

Taylor, A. M., Blurton-Jones, M., Rhee, S. W., Cribbs, D. H., Cotman, C. W., & Jeon, N. L. (2005). A microfluidic culture platform for CNS axonal injury, regeneration and transport. *Nature Methods*. https://doi.org/10.1038/nmeth777

Teixeira Lopes, A. (2018). *Spastin regulates microtubule dynamics and is required for normal motor and cognitive functions*.

Twiss, J. L., Kalinski, A. L., Sachdeva, R., & Houle, J. D. (2016). Intra-axonal protein synthesis – a new target for neural repair? *Neural Regeneration Research*, *11*(9), 1365. https://doi.org/10.4103/1673-5374.191193

Van De Velde, H. J. K., Roebroek, A. J. M., Senden, N. H. M., Ramaekers, F. C. S., & Van De Ven, W. J. M. (1994). NSP-encoded reticulons, neuroendocrine proteins of a novel gene family associated with membranes of the endoplasmic reticulum. *Journal of Cell Science*, *107*(9), 2403–2416. https://doi.org/10.1242/JCS.107.9.2403

Van Zundert, G. C. P., Rodrigues, J. P. G. L. M., Trellet, M., Schmitz, C., Kastritis, P. L., Karaca, E., Melquiond, A. S. J., Van Dijk, M., De Vries, S. J., & Bonvin, A. M. J. J. (2016). The HADDOCK2.2 Web Server: User-Friendly Integrative Modeling of Biomolecular Complexes. *Journal of Molecular Biology*, *428*(4), 720–725. https://doi.org/10.1016/J.JMB.2015.09.014

Voeltz, G. K., Prinz, W. A., Shibata, Y., Rist, J. M., & Rapoport, T. A. (2006). A class of membrane proteins shaping the tubular endoplasmic reticulum. *Cell*, *124*(3), 573–586. https://doi.org/10.1016/j.cell.2005.11.047

von Kügelgen, N., & Chekulaeva, M. (2020). Conservation of a core neurite transcriptome across neuronal types and species. *Wiley Interdisciplinary Reviews: RNA*, *11*(4), e1590. https://doi.org/10.1002/WRNA.1590;CTYPE:STRING:JOURNAL

Willis, D., Ka, W. L., Zheng, J. Q., Chang, J. H., Smit, A., Kelly, T., Merianda, T. T., Sylvester, J., Van Minnen, J., & Twiss, J. L. (2005). Differential transport and local translation of cytoskeletal, injury-response, and neurodegeneration protein mRNAs in axons. *Journal of Neuroscience*. https://doi.org/10.1523/JNEUROSCI.4235-04.2005

Wu, Y., Whiteus, C., Xu, C. S., Hayworth, K. J., Weinberg, R. J., Hess, H. F., & De Camilli, P. (2017). Contacts between the endoplasmic reticulum and other membranes in neurons. *Proceedings of the National Academy of Sciences of the United States of America*. https://doi.org/10.1073/pnas.1701078114

Yap, Y. C., King, A. E., Guijt, R. M., Jiang, T., Blizzard, C., Breadmore, M. C., & Dickson, T. C. (2017). Mild and repetitive very mild axonal stretch injury triggers cystoskeletal mislocalization and growth cone collapse. *PLOS ONE*, *12*(5), e0176997. https://doi.org/10.1371/JOURNAL.PONE.0176997

Zhang, Y., Chopp, M., Liu, X. S., Kassis, H., Wang, X., Li, C., An, G., & Zhang, Z. G. (2015). MicroRNAs in the axon locally mediate the effects of chondroitin sulfate proteoglycans and cGMP on axonal growth. *Developmental Neurobiology*, *75*(12), 1402–1419. https://doi.org/10.1002/dneu.22292

Zhang, Y., Ueno, Y., Liu, X. S., Buller, B., Wang, X., Chopp, M., & Zhang, Z. G. (2013). The MicroRNA-17-92 cluster enhances axonal outgrowth in embryonic cortical neurons. *The Journal of Neuroscience : The Official Journal of the Society for Neuroscience*, *33*(16), 6885–6894. https://doi.org/10.1523/JNEUROSCI.5180-12.2013

Acknowledgments: This research was partially supported by HPC OCÉANO (FONDEQUIP Nº EQM170214) and the supercomputing infrastructure of the NLHPC (CCSS210001). Centro Nacional de Inteligencia Artificial CENIA, FB210017, BASAL, ANID.

Funding:
ANID projects Fondecyt Initiation 11220601 (A.L.); EMBO scientific exchange grant 9218; EMBO short-stay Fellowship 8263.

Author contributions.

Examples: AL, JPR
Conceptualization: AL, AC, RHM.
Methodology: AL, TA, APL, CG, CC, FB, JG, WA, AW, ACH, DC, JT,RV.
Investigation: AL, WZ, RHM, UH, CGR, ACH, AF, JPR.
Visualization: AL, CGR, AC, JT.
Supervision: AL, AC, UH, WZ, CG, APL.
Writing—original draft: AL, AC.
Writing—review & editing: AL, AC, CG, RHM, UW, CGR.

Competing interests: Authors declare that they have no competing interests.

Data and materials availability: All data needed to evaluate the conclusions in the paper will be available upon request.

1291 **Tables and Figures**

1292

Study	Neuron cell type	Model to obtain axonal fraction
(Saal et al., 2014)	Mice motor neurons	Spinal cord motor neurons cultured in microfluidic chambers (7 DIV).
(Rotem et al., 2017)	Mice motor neurons	Spinal cord motor neurons cultured in porous membrane inserts (10 DIV).
(Maciel et al., 2018)	iPSC-derived human motor neurons	Motor neurons were cultured on porous membrane inserts (10 DIV)
(Bigler et al., 2017)	Glutamatergic neurons differentiated from human embryonic stem cells (hESCs)	hESCs differentiated for 59 DIV in microfluidic chambers.
(Nijssen et al., 2018)	Human and mice motor neurons.	Spinal cord and human stem cell derived motor neurons were cultured in microfluidic chambers (7 and 14 DIV, respectively).
(Farias et al., 2020)	Rat mature myelinated motor neurons	Axoplasm microdissection of motor axons (*Ex vivo*).
(Gumy et al., 2011)	Rat embryonic/adult sensory neurons from dorsal root ganglion (DRG)	Primary neurons were cultured in microfluidic chambers (4 DIV).
(Taylor et al., 2009)	Uninjured and regenerating rat cortical neurons	Primary neurons cultured in microfluidic chambers (10 DIV).

1293 **Table I.** Analyzed publications examining the transcriptome of an axon-enriched neuronal
1294 fraction. Days *in vitro* (DIV).

1295

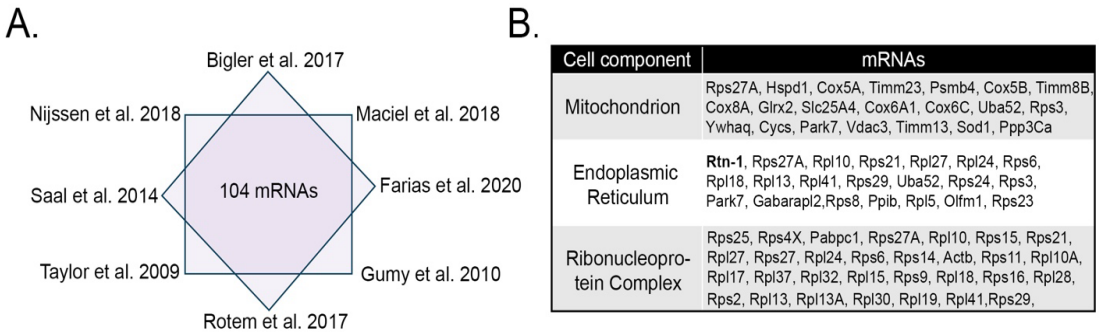

Cell component	mRNAs
Mitochondrion	Rps27A, Hspd1, Cox5A, Timm23, Psmb4, Cox5B, Timm8B, Cox8A, Glrx2, Slc25A4, Cox6A1, Cox6C, Uba52, Rps3, Ywhaq, Cycs, Park7, Vdac3, Timm13, Sod1, Ppp3Ca
Endoplasmic Reticulum	**Rtn-1**, Rps27A, Rpl10, Rps21, Rpl27, Rpl24, Rps6, Rpl18, Rpl13, Rpl41, Rps29, Uba52, Rps24, Rps3, Park7, Gabarapl2,Rps8, Ppib, Rpl5, Olfm1, Rps23
Ribonucleoprotein Complex	Rps25, Rps4X, Pabpc1, Rps27A, Rpl10, Rps15, Rps21, Rpl27, Rps27, Rpl24, Rps6, Rps14, Actb, Rps11, Rpl10A, Rpl17, Rpl37, Rpl32, Rpl15, Rps9, Rpl18, Rps16, Rpl28, Rps2, Rpl13, Rpl13A, Rpl30, Rpl19, Rpl41,Rps29,

1296

1297 **Figure 1. Analysis of diverse axonal transcriptomes reveals that *Rtn-1* mRNA is consistently**
1298 **identified**. **A.** Scheme illustrates studies of axonal transcriptomes and 104 shared mRNAs
1299 identified using Venn analysis. **B.** Table lists the category "Cellular Component" (Gene Ontology,
1300 GO) to classify the proteins coded by the 104 common mRNAs. The endoplasmic reticulum (ER)
1301 category only harbors *Rtn-1* (bold) as the only common mRNA coding for an ER structural
1302 protein.

1303

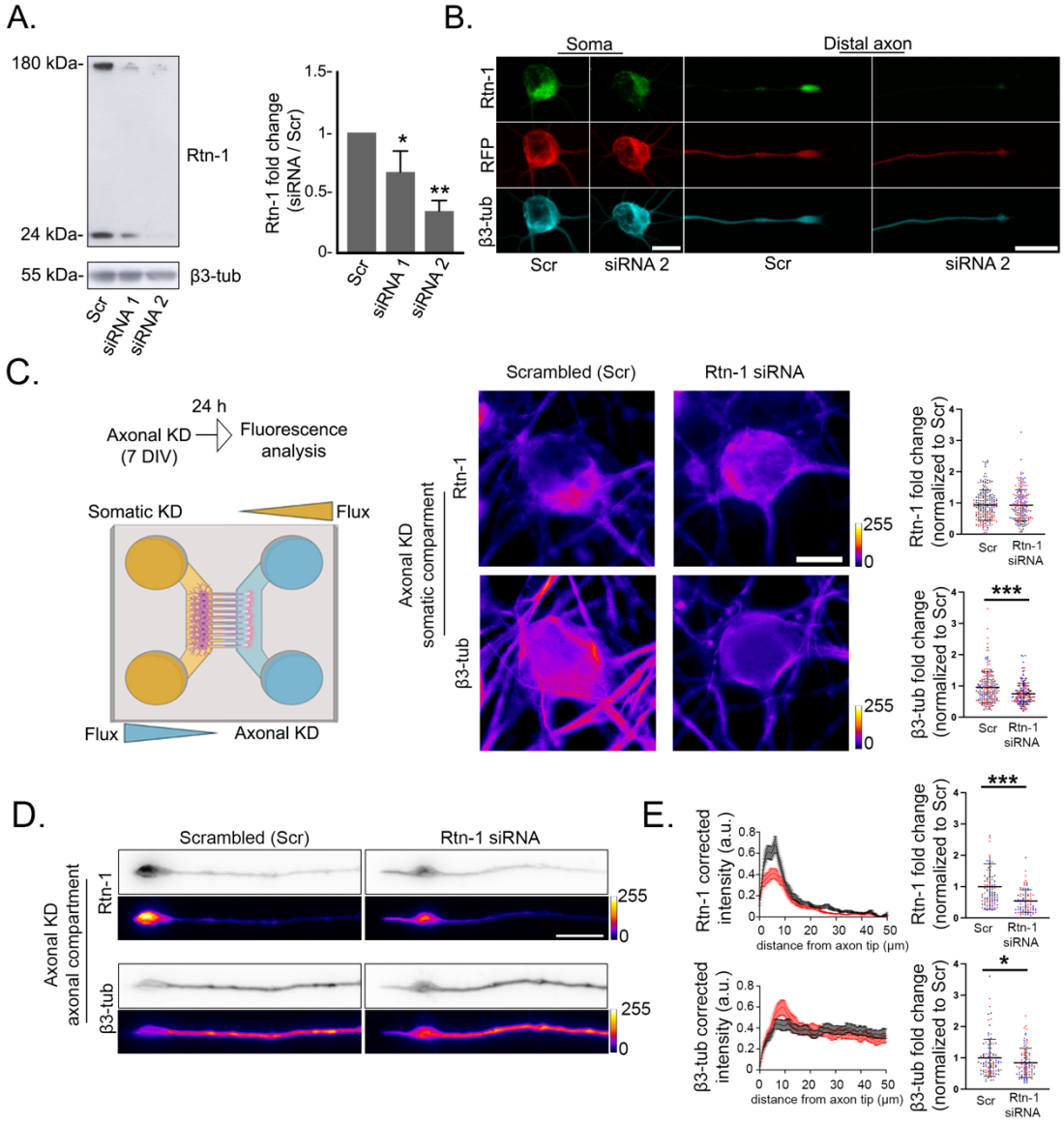

Figure 2. Axonal synthesis of Rtn-1 can be locally regulated in cortical neurons. A. *Left:* Western blot bands of Rtn-1 and β3-tubulin (β3-tub) confirms the knockdown (KD) efficacy of siRNAs specifically designed against *Rtn-1* mRNA (Rtn-1 siRNA). 7 DIV Cortical neurons were transfected with Rtn-1 siRNAs and a control sequence (scrambled, Scr) for forty-eight hours. 20 µg of protein were loaded per lane, and β3-tubulin was used as loading control. *Right:* Graphs quantify the fold change of the 24 kDa Rtn-1 band after treatments with siRNAs 1-2 compared to Scr. Data are displayed as mean ± standard error of N = 6 biological replicates. Wilcoxon test compared to a theoretical mean of 1; $*p < 0.05$; $**p < 0.01$. **B.** Immunofluorescence images of the soma and distal axon of neurons stained against β3-tub and co-transfected with a plasmid encoding RFP and siRNA 2 or Scr under the same conditions indicated in A. Representative images from N = 4 biological replicates**.** Bar soma and axons = 20 µm **C.** *Left:* schematic representation of the axonal KD strategy based on controlling volume differences between the compartment of microfluidic chambers. Under these conditions, 7 DIV cortical neurons were

selectively submitted to axonal treatments for twenty-four hours. *Right:* representative images and quantitative analysis of Rtn-1 and β3-tub intensity fold change in the cell bodies after axonal treatments. Bar = 10 µm. Data are displayed as mean ± standard deviation (SD) of 229-300 neurons from N = 3 biological replicates. Linear mixed-effects model with experimental date included as a random effect; $***p < 0.001$. **D.** Immunofluorescence showing the intensity changes of Rtn-1 and β3-tubulin along the last 50 µm of axons locally treated with Rtn-1 siRNA or Scr. Bar =10 µm **E.** *Left:* corrected fluorescence intensity profiles of Rtn-1 and β3-tubulin from the last 50 µm of distal axons locally treated with Rtn-1 siRNA (red line) or Scr (black line). Intensity profiles depict the mean ± standard error from all the analyzed axons. *Right:* Bar graphs display the mean ± standard deviation of the fluorescence intensity fold change of 87-102 axons from N = 3 biological replicates. Linear mixed-effects model with experimental date included as a random effect; $*p < 0.05$; $***p < 0.001$.

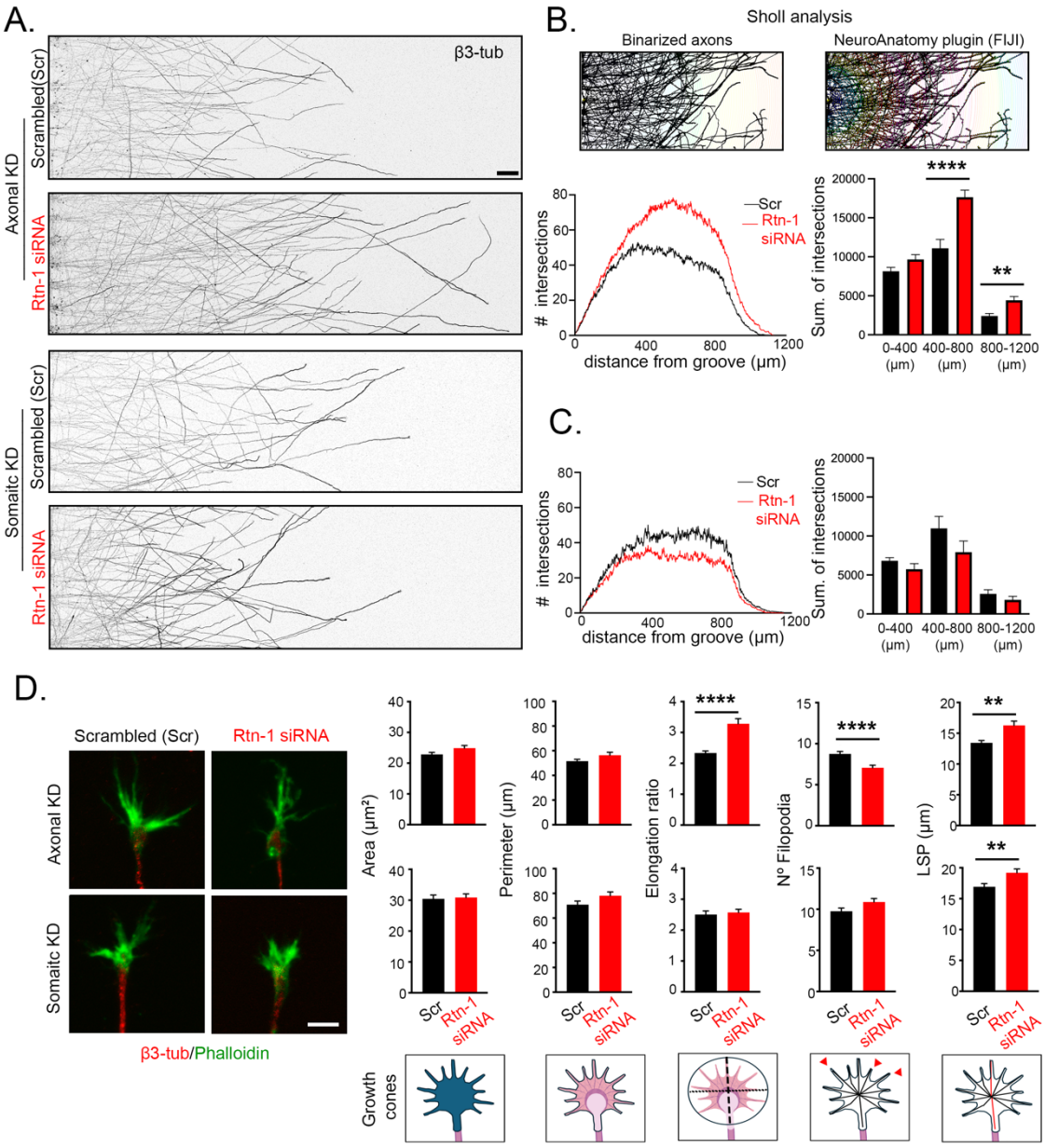

Figure 3. Axonal Rtn-1 knockdown (KD) promotes outgrowth and modify growth cone (GC) cytoskeleton after injury. A. Immunofluorescence against β3-tubulin in axons growing in microfluidic chambers twenty-four hours after injury (vacuum aspiration axotomy) comparing axonal and somatic Rtn-1 KD performed with a specific siRNA (Rtn-1-siRNA) or control sequence (scrambled, Scr). Bar = 50 µm. **B.** *Top:* schematic of the Sholl analysis performed with the NeuroAnatomy plugin (FIJI). The number of intersections of binarized axons (*left)* with concentric semi-circles of increasing radius starting in the microgroove at the center of each axonal field were quantified (*right*). *Bottom:* mean plots of the Sholl analyses performed after axonal Rtn-1 KD (red line) compared to Scr (black line). Bar graphs show the summation (sum.) of the total intersections within the indicated distance bins. **C.** Same analysis as in panel B but performed for somatic Rtn-1 KD. Data are displayed as mean ± standard error of 23-24 axonal fields from N = 6 biological replicates for axonal Rtn-1 KD; and 18-20 axonal fields from N = 3

biological replicates for somatic Rtn-1 KD. Two-tailed Mann–Whitney *U* test; **p < 0.01; ****p < 0.0001.**C.** Images show axonal growth cones after axonal or somatic Rtn-1 KD compared to Scr labeled against β3-tubulin (red) and Phalloidin (green) for staining the F-actin outline. Bar = 5 µm. Graphs depict the corresponding differences in GC area, perimeter, elongation ratio (or aspect ratio), number of filopodia, and longest shortest path (LSP), which corresponds to maximal distance calculated from the skeletonized outline (shown with the red line of the schematic drawings below). Data are displayed as mean ± standard error of 145-153 axons for axonal KD; 227-148 axons for somatic KD from N = 3 biological replicates. Two-tailed Mann–Whitney *U* test; ∗∗p < 0.01; ∗∗∗∗p < 0.0001.

1353

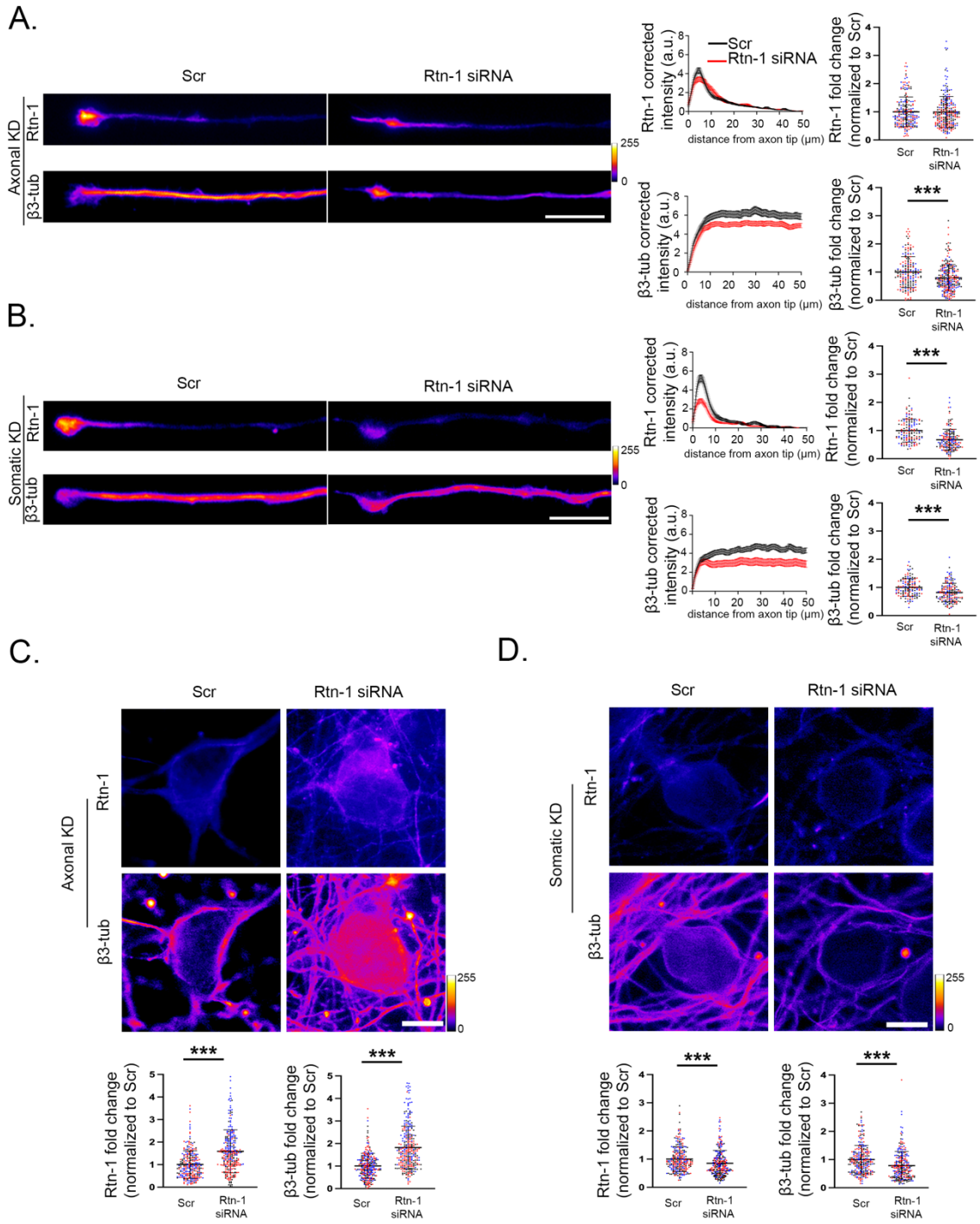

1354

1355 **Figure 4. Axonal and somatic β3-tubulin levels are dependent on the local synthesis of Rtn-**
1356 **1 after injury. A.** *Left:* immunofluorescence images and their corresponding corrected
1357 fluorescence intensity profiles along the last 50 μm of distal axons stained against Rtn-1 and β3-
1358 tubulin after axonal transfection with Rtn-1 siRNA (red; axonal Rtn-1 KD) or a control sequence
1359 (black; scrambled, Scr). Intensity profiles depict the mean ± standard deviation from all the
1360 analyzed axons. Bar = 10 μm. *Right:* bar graphs quantify the Rtn-1 and β3-tubulin (β3-tub)
1361 fluorescence intensity fold change. Data are displayed as the mean ± standard deviation of 206–

242 axons from N = 3 biological replicates. Linear mixed-effects model with experimental date included as a random effect; ***$p < 0.001$.**B.** Same analysis as in panel A but performed for somatic Rtn-1 KD. Data are displayed as mean ± standard error of 133–161 axons from N = 3 biological replicates. Linear mixed-effects model with experimental date included as a random effect; ***$p < 0.001$. **C.** Images depict neuronal cell bodies stained for Rtn-1 and β3-tub after axonal Rtn-1 KD or Scr. Bar graphs depict Rtn-1 and β3-tub fluorescence intensity fold change displayed as mean ± standard error of 358–382 neurons from N = 3 biological replicates. Linear mixed-effects model with experimental date included as a random effect; ***$p < 0.001$. Bar = 10 µm. **D.** Same analysis as in panel C but performed for somatic Rtn-1 KD. Data are displayed as mean ± standard error of 252–237 neurons from N = 3 biological replicates. Linear mixed-effects model with experimental date included as a random effect; ***$p<0.001$. Bar = 10 µm.

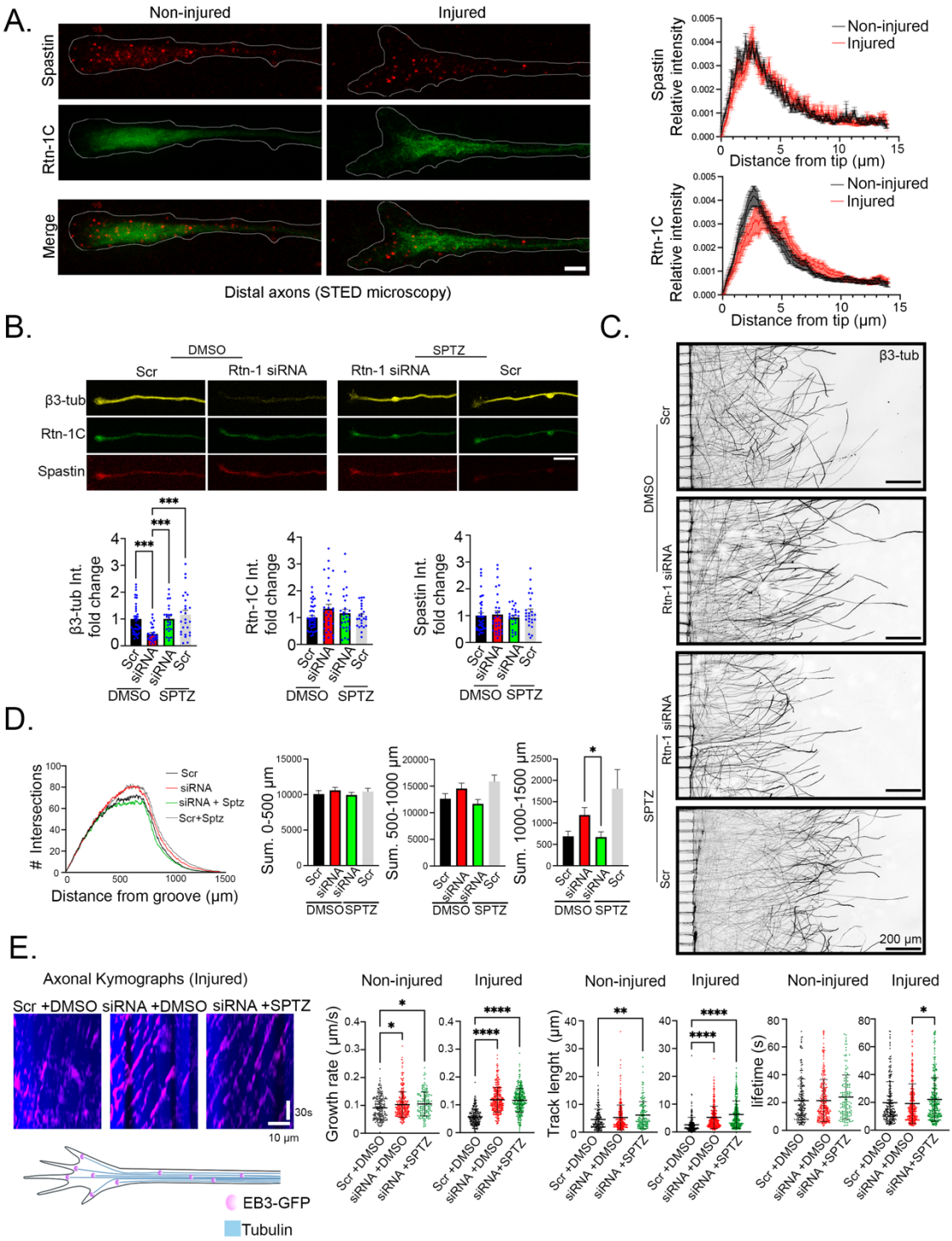

Figure 5. Axonal Rtn-1 KD after injury controls distal tubulin levels and outgrowth depending on Spastin microtubule severing. **A.** *Left:* representative fluorescent super resolution STED images of distal non-injured and injured cortical axons (forty-four hours post-axotomy) in microfluidic chambers, which were stained against Rtn-1C (green), and Spastin (red), axon outlines are depicted (white lines). *Right:* Plots depict the relative fluorescence intensity profile (normalized against total distal intensity) of Rtn-1C and Spastin in non-injured (black) and injured (red) axons. Data are displayed as mean ± standard error of 9-13 axons from N = 4 biological

replicates. Bar = 5 µm **B.** *Top:* representative confocal images of distal axons stained against β3-tubulin (β3-tub, yellow), Rtn-1C (green), and Spastin (red) in microfluidic chambers forty-four hours post-axotomy under indicated treatments: control (Scrambled, Scr), axonal Rtn-1 KD (Rtn-1 siRNA), and Spastin pharmacological inhibition with 50 nM Spastazoline (SPZT) or vehicle (DMSO). Bar = 10 µm. *Bottom:* quantifications of fluorescence intensity fold change of indicated proteins in the last 50 µm normalized to Scr + DMSO. Data are displayed as mean ± standard error of 24-40 axons for condition from N = 3 biological replicates. Kruskal–Wallis followed by Dunn's post hoc test; ∗∗∗$p < 0.001$.**C.** Illustrative axonal fields in microfluidic chambers forty-four hours post-axotomy stained against β3-tub under the treatments shown in B. Bar = 200 µm. **D.** *Left:* mean plots of the Sholl analyses performed with colored lines indicating the analyzed conditions. *Right:* bar graphs show the summation (Sum.) of the total intersections within the indicated distance bins. Data are displayed as mean ± standard error of 22-24 axonal fields for condition from N = 3 biological replicates. One-way ANOVA followed by Tukey's post hoc test; ∗$p < 0.05$. **E.** *Left:* axonal kymographs showing microtubule dynamics in neurons with indicated treatments forty-four hours after axotomy, dashes represent the traces of EB3-GFP (end-binding protein 3 fused to Emerald GFP). Scale bars represent 10 µm and 30 seconds, respectively. *Right:* bar graphs show microtubule dynamic parameters in non-injured and injured axons with indicated treatments. Data are displayed as mean ± standard error of 146-377 comets/dashes for condition from N = 3 biological replicates. Kruskal–Wallis followed by Dunn's post hoc test; ∗$p < 0.05$; ∗∗$p < 0.01$; ∗∗∗∗$p < 0.001$.

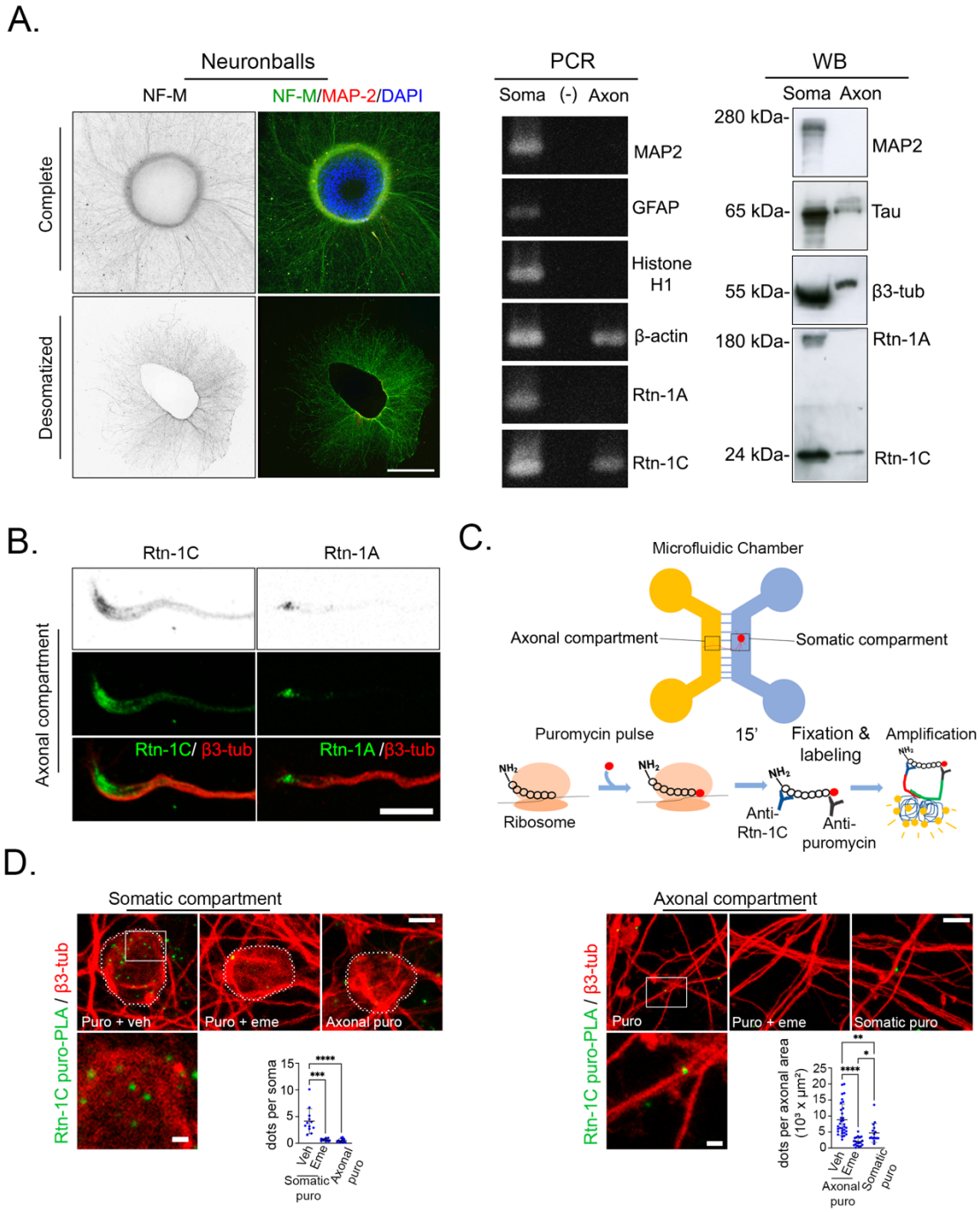

Figure 6. **Rtn-1C is locally synthesized in cortical axons**. **A.** *Left:* immunofluorescence of neuronballs stained against neurofilament medium chain (NF-M, grayscale and green) and Microtubule-associated protein 2 (MAP2, grayscale and red) with nuclei counterstaining (DAPI, blue). Top panel shows intact neuronballs, bottom panel shows them after mechanic removal of the cell bodies. *Middle:* RT- PCR bands of somatic (soma), axonal (Axon), and (-) (reaction of axonal RNA without reverse transcriptase) to reveal mRNAs coding for MAP2, glial fibrillary acidic protein (GFAP), Histone H1, β-actin, Rtn-1C, and Rtn-1A. *Right:* Western blot analysis of the corresponding fractions using a pan-Rtn-1 antibody to reveal Rtn-1A and Rtn-1C isoforms, β3-tubulin (β3-tub), and Tau. Bar = 500 µm. Images and bands are representative of two

biological replicates. **B.** Confocal images showing the expression of Rtn-1C and Rtn-1A (green) and β3-tub (red) in the distal axonal compartment of microfluidic chambers. Bar = 10 µm. Images are representative of two biological replicates **C.** Schematic of the microfluidic chamber setup used to perform proximity ligation assay coupled to puromycylation (puro-PLA) is depicted below. Local puromycin (puro) incorporation into newly synthesized peptides allows amplification when puro is at nanometric distance from the N-terminal. **D.** puro-PLA positive spots are shown in green at somatic and axonal compartments. β3-tub labeling depicts cell bodies and axons. Insets show higher magnification of puro-PLA signals. Bar graphs quantify dots per cell bodies and per axonal area after local co-treatments of puro with the protein synthesis inhibitor emetine (Eme) or vehicle (Veh), or puro at the opposite compartment. Bar = 5 µm; inserts= 1 µm. Data are displayed as mean ± standard deviation of 11-12 somatic and 16-33 axonal fields from N = 4 biological replicates. Kruskal–Wallis followed by Dunn´s post hoc test; *$p < 0.05$; **$p < 0.01$; ***$p < 0.001$; **** $p < 0.0001$.

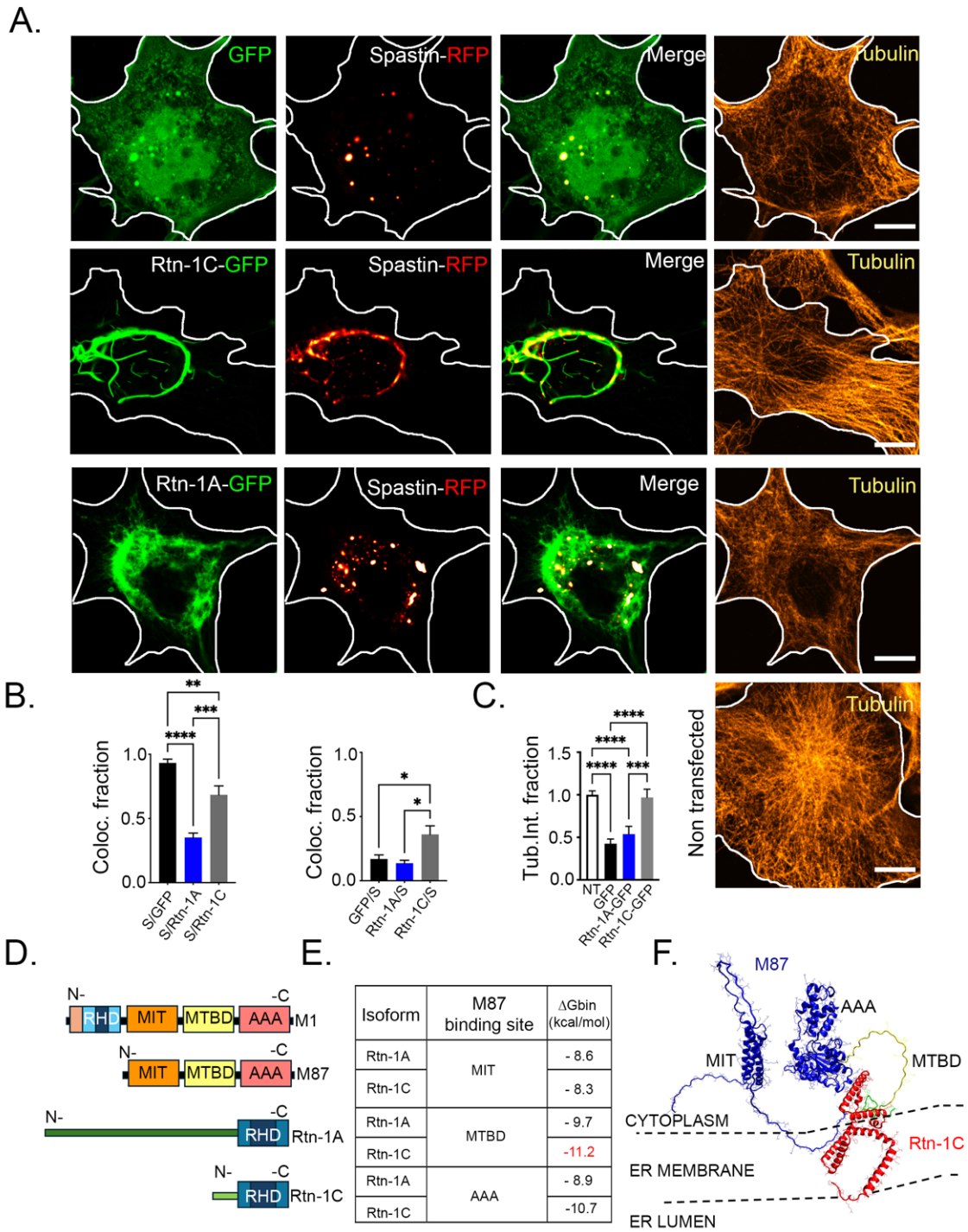

Isoform	M87 binding site	ΔGbin (kcal/mol)
Rtn-1A	MIT	- 8.6
Rtn-1C		- 8.3
Rtn-1A	MTBD	- 9.7
Rtn-1C		-11.2
Rtn-1A	AAA	- 8.9
Rtn-1C		-10.7

Figure 7. Rtn-1C co-distributes with Spastin and attenuates its microtubule-severing activity. A. Representative images of COS-7 cells expressing Spastin-RFP (fire red) together with GFP (green), Rtn-1A-GFP, or Rtn-1C-GFP, and immunostained against tubulin (yellow). Bar =10 µm. **B.** Bar graphs show the indicated Mander's coefficients to quantify the colocalization between Spastin-RFP and GFP or Rtn-1 isoforms. Data are displayed as mean ± standard error from 9 cells per condition from N = 2 biological replicates. One-way ANOVA with Tukey's post hoc test; *$p < 0.05$, **$p < 0.01$, ****$p < 0.0001$. **C.** Tubulin intensity fraction normalized to non-transfected cells (NT) in cells expressing Spastin-RFP with GFP, Rtn-1A-GFP, or Rtn-1C-GFP

1436 compared to non-transfected cells. Data are displayed as mean ± standard error from 145 non-
1437 transfected cells, 33 Spastin-RFP/GFP cells, 35 Spastin-RFP/Rtn-1A-GFP cells, and 32 Spastin-
1438 RFP/Rtn-1C-GFP cells from N = 2 biological replicates. One-way ANOVA with Tukey's post
1439 hoc test; *$p < 0.05$, **$p < 0.01$, ***$p < 0.001$, ****$p < 0.0001$. **D.** Domain organization of Spastin
1440 isoforms (M1 and M87) and Rtn-1 isoforms (Rtn-1A and Rtn-1C), including the Reticulon
1441 Homology Domain (RHD), Microtubule Interacting and Trafficking domain (MIT), Microtubule-
1442 Binding Domain (MTBD), and ATPases Associated with diverse cellular Activities (AAA)
1443 domain (severing domain). **E.** Predicted binding affinities (ΔG binding, kcal/mol) between
1444 Spastin M87 and Rtn-1 isoforms at different domains, highlighting strong interactions with Rtn-
1445 1C. **F.** Structural model (VMD snapshots) of the predicted interaction between the MTBD
1446 (yellow) of Spastin M87 (blue) and the N-terminal region (green) of Rtn-1C (red).

Supplementary Figures

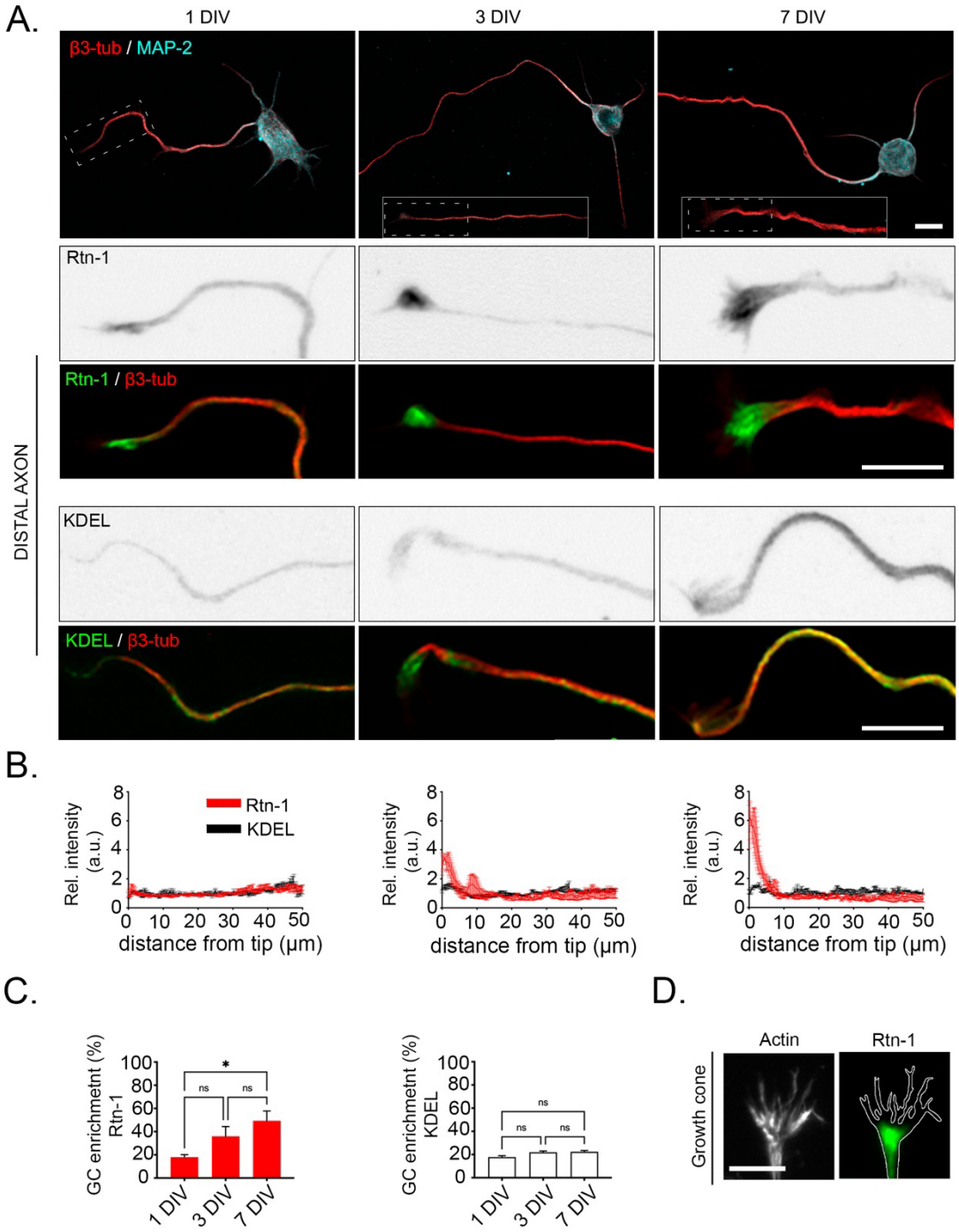

Supplementary figure 1. Rtn-1 is progressively enriched in the growth cone (GC) of developing cortical neurons. A. *Top:* immunofluorescence images showing the distribution of Rtn-1 and microtubule-associated protein 2 (MAP2) in cultured cortical neurons at 1, 3, and 7 days *in vitro* (DIV). Bar = 10 µm. *Bottom:* co-labeling of Rtn-1 or KDEL (green) with β3-tubulin (β3-tub, red) depicts the endoplasmic reticulum in distal axons. Bar = 10 µm **B.** Intensity profiles indicate the relative intensity (Rel. intensity, normalized against the total fluorescence) of Rtn-1 and KDEL in distal axons. Data are displayed as mean ± standard error of 80–100 axons from N = 3 biological replicates. **C.** Bar graphs quantify the percentage of total Rtn-1 and KDEL

fluorescence present in the first 10 µm of axons (GC) at 1, 3 and 7 DIV. Data are displayed as mean ± standard error of 80–100 axons from N = 3 biological replicates. ∗p < 0.05; n.s., not significant; One-way ANOVA followed by Tukey's post hoc test. **D.** Representative image of Rtn-1 distribution (green) at the GC identified with the F-actin outline (grays) stained with phalloidin. Bar = 5 µm.

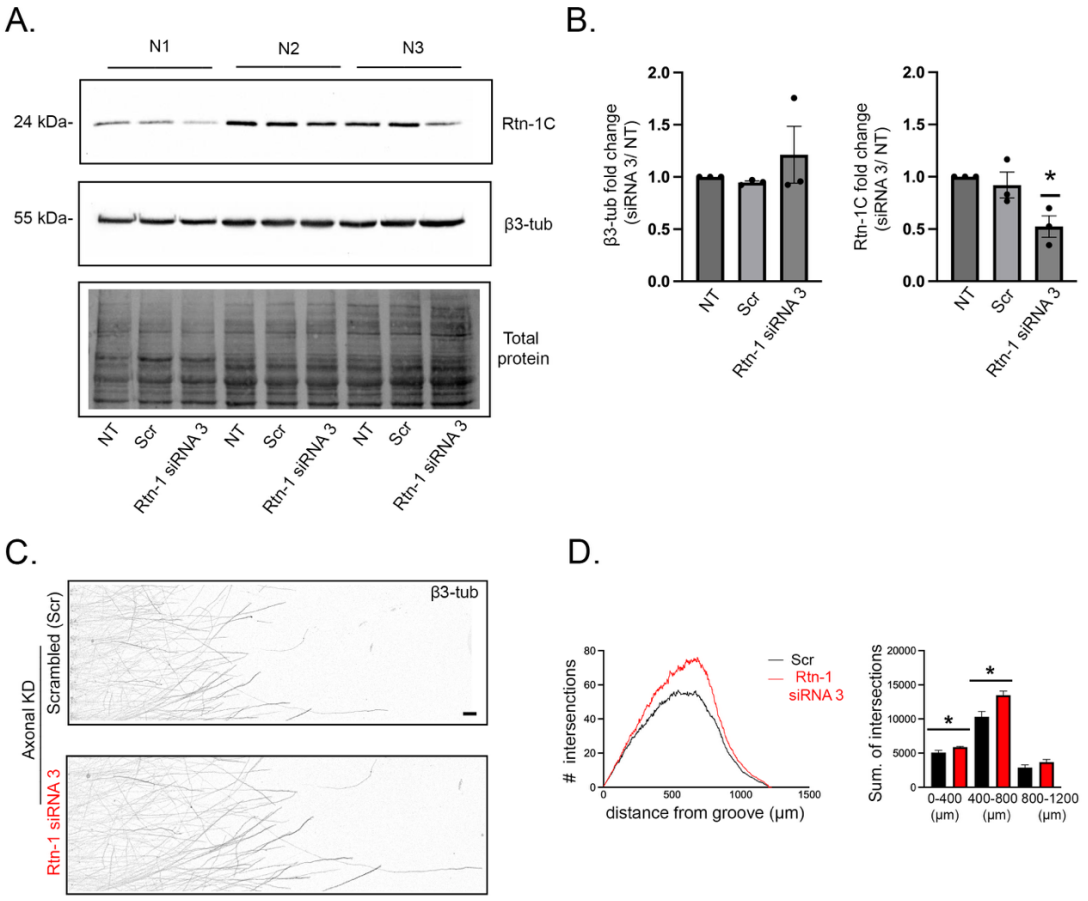

Supplementary figure 2. Axonal knockdown (KD) of Rtn-1 with a different siRNA reproduced increased outgrowth. A. Representative Western blot of Rtn-1C and β3-tubulin (β3-tub) in three independent 7 day *in vitro* (DIV) cortical neuron cultures (N1–N3) transfected with siRNA 3 directed against Rtn-1 (Rtn-1 siRNA 3) and a control sequence (scrambled, Scr) for forty-eight hours. 9 DIV, non-transfected (NT) cells were also analyzed. Total protein staining was used as a loading control. **B.** Bar graphs quantify the fold change in β3-tub (left) and Rtn-1C (right) levels relative to NT. Data are displayed as the mean ± standard error from N = 3 biological replicates. Wilcoxon test compared to a theoretical mean of 1; ∗p < 0.05 **C.** Representative images of axonal fields stained against β3-tub in microfluidic chambers after axonal KD with Rtn-1 siRNA 3 or Scr. Bar = 50 µm.**D.** *Left:* mean plots of the Sholl analyses performed after axonal Rtn-1 KD (red) compared to Scr (black). *Right:* Bar graphs indicate the summation (sum.) of intersections within the defined distance bins. Data are displayed as the mean ± standard error of

23-30 axonal fields from N =3 biological replicates. Unpaired Student's t Test; *p < 0.05; **p < 0.01.

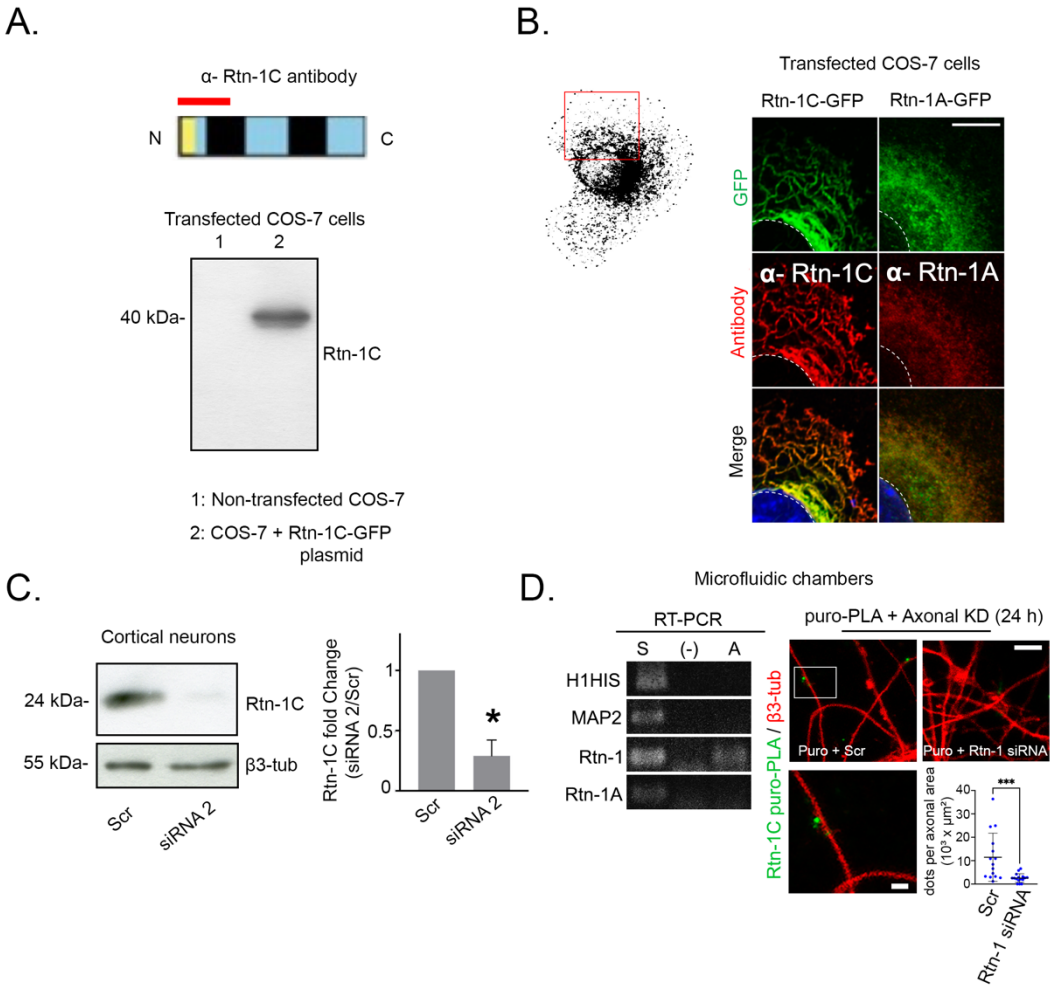

Supplementary figure 3. Validation of Rtn-1C antibody specificity and puro-PLA signal by axonal knockdown (KD) of Rtn-1. A. *Top:* Schematic of the epitope (red bar) within the N-terminal region of Rtn-1C (top). *Bottom:* Western blot analysis of COS-7 cells non-transfected (lane 1) or transfected with Rtn-1C-GFP (lane 2). **B.** Immunofluorescence validation of α-Rtn-1C and α-Rtn-1A antibodies in COS-7 cells transfected with Rtn-1C-GFP (left) or Rtn-1A-GFP (right). Bar = 20 µm.**C.** *Left:* Western blot of 7 days *in vitro* (DIV) cortical neurons transfected for forty-four hours with siRNA targeting Rtn-1 (siRNA 2) or control sequence (scrambled, Scr). *Right:* Bar graphs quantify the intensity fold change of Rtn-1C versus Scr (normalized to β3-tubulin). Data are displayed as mean ± standard error from N = 3 biological replicates. *p < 0.05; Wilcoxon test compared to a theoretical mean of 1.**D.** *Left:* RNA was isolated from 8 DIV microfluidic chamber compartments and submitted to RT- PCR. Bands depict somatic (S), axonal (A) and negative control corresponding to axonal samples without reverse transcriptase (-). *Top right:* 8 DIV cortical axons were locally treated with siRNA 2 and Scr for twenty-four hours and then submitted to puromycylation proximity ligation assay (puro-PLA) to reveal local Rtn-1C

synthesis (green puncta) along β3-tubulin–positive axons (red). Bar = 5 µm Bar insert = 2.5 µm. *Bottom right:* Bar graphs quantify the number of positive dots per axonal area. Data are displayed as the mean ± standard deviation of 15-16 axonal fields from N = 3 biological replicates. Mann–Whitney test; ***p < 0.001.

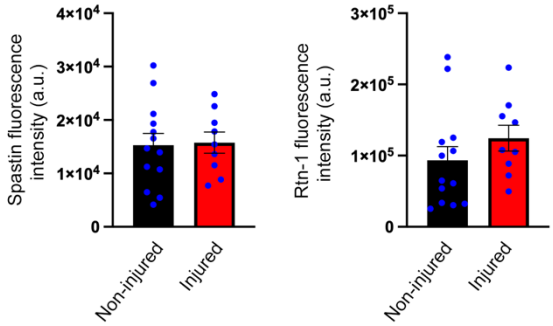

Supplementary figure 4. Distal axonal levels of Spastin and Rtn-1C are not altered by axotomy. Quantification of the fluorescence intensity for Spastin (left) and Rtn-1C (right) in distal (last 15 µm) non-injured (black) and injured (red) axons in microfluidic chambers as described in Figure 5. Data are displayed as mean ± standard error of 9-13 axons from N = 3 biological replicates. No significant differences were detected between conditions.

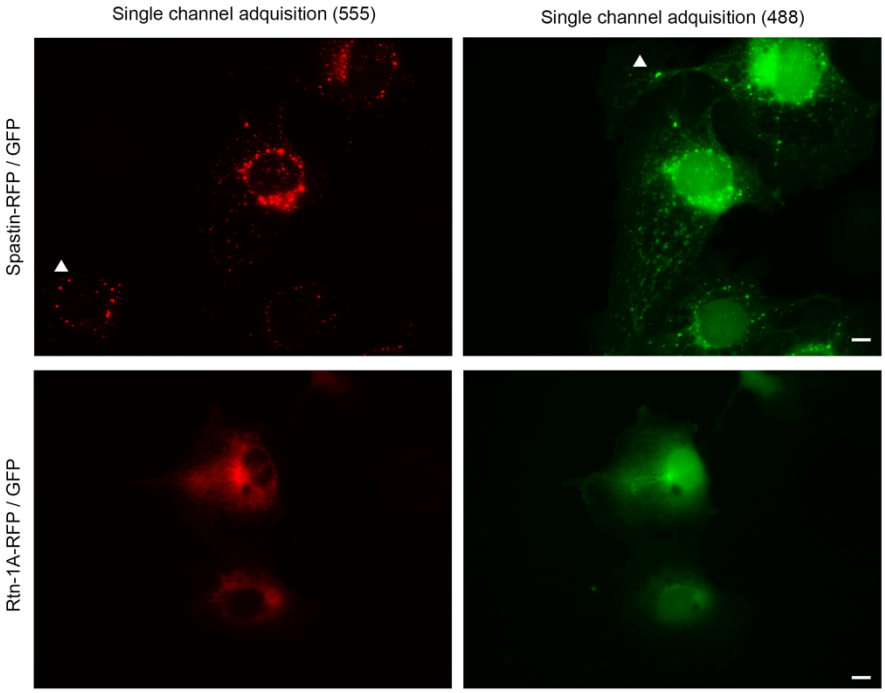

Supplementary figure 5. Single-channel acquisition confirms punctate distribution of Spastin-RFP and GFP in co-transfected COS-7 cells. *Top:* COS-7 cells were co-transfected with Spastin-RFP (left, 555 channel) and GFP (right, 488 channel). Spastin-RFP displays a

punctate distribution that strongly co-distributes with GFP puncta. Independent acquisition of each channel demonstrates that this overlap is not due to fluorescence crosstalk, since some puncta appear exclusively in one channel (arrowheads). *Bottom:* Cells transfected with Rtn-1A-RFP and GFP show distinct distribution patterns supporting absence of crosstalk. Bar = 5 µm.

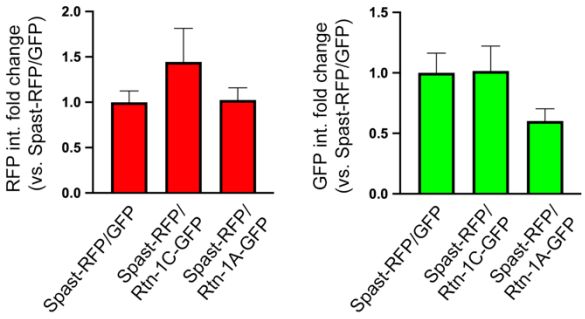

Supplementary figure 6. **Expression levels of Spastin and Rtn-1 constructs are comparable across analyzed cells.** Quantification of fluorescence intensity for RFP (left) and GFP (right) signals in cells co-expressing Spastin-RFP with GFP, Rtn-1C-GFP, or Rtn-1A-GFP, corresponding to the experimental conditions described in Figure 7. Data are displayed as mean ± standard error of 33 Spastin-RFP/GFP cells; 35 Spastin-RFP/Rtn-1A-GFP cells; and 32 Spastin-RFP/Rtn-1C-GFP cells from N = 2 biological replicates. Kruskal–Wallis followed by Dunn's post hoc test. No significant differences were found across conditions.

Reagent tables

Primary Antibodies

Antibody	Cat. Nº	Company	Host	Description	Dil. IF	Dil. WB
Reticulon-1C	sc-23882	Santa Cruz	Mouse		1:50	1:500
Reticulon-1C	ab8961	Abcam	Mouse	Proximity ligation assay and Western blot	1:1000	--
Reticulon-1A	AB 9274	Abcam	Mouse		1:500	
Reticulon-1 (All isoforms)	ab83049	Abcam	Rabbit		1:500	1:1000
Spastin	PA5-53581	Invitrogen	Rabbit		1:500	--
KDEL	PA1-013	Thermo Fisher	Rabbit		1:200	
MAP2	M3696	Sigma	Rabbit		--	1:500
MAP2	MAB3418	Millipore	Mouse		1:500	--
β3-tubulin	NB100-1612	Novus	Chicken		1:2000	
β3-tubulin	2G10	Abcam	Mouse	Neuronball Western blots	--	1:5000
NF-M	AB 1987	Millipore	Rabbit		1:500	
Puromycin	3RH1	Kerafast	Mouse		1:200	--
Tau	MAB3420	Chemicon	Mouse			1:1000
Phalloidin	A12379	Thermo Fisher	--	Growth cone staining	1:500	

Secondary Antibodies

Antibody	Cat. Nº	Company	Host	Description	Dil. IF	Dil. WB
Alexa Fluor® 488 anti mouse	a21202	Thermo Fisher	Donkey		1:1000	--
Alexa Fluor® 555 anti rabbit	a21429	Thermo Fisher	Goat		1:1000	--
Alexa Fluor® 488 anti rabbit	a11034	Thermo Fisher	Goat		1:1000	--
Alexa Fluor® 647 anti chicken	A-21449	Thermo Fisher	Goat		1:1000	--
Anti-Rabbit IgG - Atto 594	77671	Sigma, Aldrich	Goat	Used for experiments with STED	1:500	--
Anti-Mouse −Atto 488	62197	Sigma, Aldrich	Goat	Used for experiments with STED	1:500	--
anti-mouse anti-IgG	31430	Thermo Fisher	Goat	horseradish peroxidase	--	1:5000

				conjugated antibody		
anti-rabbit IgG	31460	Thermo Fisher	Goat	horseradish peroxidase conjugated antibody	--	1:5000
anti-Chicken IgG	SAB3700195	Sigma-Aldrich	Goat	horseradish peroxidase conjugated antibody	--	1:5000

Plasmids

Gene	Backbone	Reporter	Promoter
Rat RTN1A Gene ORF (NM_053865.1)	pCMV3-C-GFPSpark	GFP	CMV (Over expression)
Rat RTN1C Gene ORF (XM_008764690)	pCMV3-C-GFPSpark	GFP	CMV (Over expression)
Rat SPAST Gene ORF (NM_001108702.2)	pCMV3-C-ORFSpark	ORF	CMV (Over expression)
pCMV3-C-GFPSpark Control Vector	pCMV3-C-GFPSpark	GFP	CMV (Over expression)
Rat EB3 Gene ORF (NM_012326.2)	mEmerald-C1	mEmerald-C1 (GFP)	CMV (Over expression)

Primers

Gene	Forward	Reverse
H1 histone	5’-ACCCATTGTTCAAGGACAGC-3’	5’-ATCAGGTCCCCCAACTTACC-3’
β-actin	5’-AGCCATGTACGTAGCCATCC-3’	5’- CTCTCAGCTGTGGTGGTGAA-3’
Reticulon-1	5`-GAGCAGATCCAGAAGTACAC- 3’	5’-GAAACCACAGCCATAAGCAG-3’
Reticulon-1A	5’- ATGGAAACTGCATCCACA-3’	5’-AAAAGTATGCAGAGTCCTC-3’
Reticulon-1C	5’-ACCATGCAGGCCACTGCCGATTC-3’	5’-CTCAGCGTGCCTCTTGGCGCC-3’
GFAP	5’-GGCGCTCAATGCTGGCTTCA-3’	5’-TCTGCCTCCAGCCTCAGGTT-3’

Oligonucleotides

Oligo	+ Strand	-Strand
siRNA 1	5'rGrArArArArGrUrCrArGrGrCrUrArUrUrGrArCrCrUrUrCrTrG 3'	5'rCrArGrArArGrGrUrCrArArUrArGrCrCrUrGrArCrUrUrUrUrCrCrA 3'
siRNA 2	5’rCrGrArUrGrUrUrUrArCrUrCrUrArCrCrUrGrUrGrGrUrATA 3’	5’rUrArUrArCrCrArCrArGrGrUrArArArCrArUrCrGrArA 3’
siRNA 3	5'rGrUrGrGrUrUrUrCrGrArUrGrUrUrUrArCrUrCrUrArCrCTG 3'	5'rCrArGrGrUrArGrArGrUrArArArCrArUrCrGrArArArCrCrArCrArG 3'
IDT Negative Control DsiRNA (51-01-14-03)		